SHANK proteins limit integrin activation by directly interacting with Rap1 and R-Ras

Johanna Lilja[#1], Thomas Zacharchenko[#2], Maria Georgiadou[1], Guillaume Jacquemet[1], Nicola De Franceschi[1], Emilia Peuhu[1], Hellyeh Hamidi[1], Jeroen Pouwels[1], Malte Beifuss[3], Victoria Martens[3], Fatemeh Hassani Nia[3], Tobias Boeckers[4], Hans-Juergen Kreienkamp"[3], Igor Barsukov"[2] and Johanna Ivaska"[1, 5]

[1]Turku Centre for Biotechnology, University of Turku, FIN-20520 Turku, Finland

[2]University of Liverpool, Liverpool, United Kingdom

[3]Institute for Human Genetics, University Medical Center Hamburg-Eppendorf, Hamburg, Germany

[4]Institute for Anatomy and Cell Biology, University of Ulm, Ulm, Germany

[5]Department of Biochemistry and Food Chemistry, University of Turku, Turku, Finland

[#]equal contribution

"corresponding authors Hans-Jürgen Kreienkamp (Kreienkamp@uke.de), Igor Barsukov (I.Barsukov@liverpool.ac.uk) and Johanna Ivaska (Johanna.ivaska@utu.fi)

Abstract

SHANK3, a synaptic scaffold protein and actin regulator, is widely expressed outside of the central nervous system with predominantly unknown function. Solving the structure of the SHANK3 N-terminal region revealed that the SPN-domain is an unexpected Ras-association domain with high affinity for GTP-bound Ras and Rap G-proteins. The role of Rap1 in integrin activation is well established but the mechanisms to antagonize it remain largely unknown. Here, we show that SHANK1 and SHANK3 act as integrin activation inhibitors by sequestering active Rap1 and R-Ras via the SPN-domain and thus limiting their bioavailability at the plasma membrane. Consistently, *SHANK3* silencing triggers increased plasma membrane Rap1 activity, cell spreading, migration and invasion. Autism-related mutations within the SHANK3 SPN-domain (R12C and L68P) disrupt G-protein interaction and fail to counteract integrin activation along the Rap1/RIAM/talin axis in cancer cells and neurons. Altogether, we establish SHANKs as critical regulators of G-protein signalling and integrin-dependent processes.

Introduction

Integrins are heterodimeric transmembrane receptors that couple the extracellular matrix (ECM) to the actin cytoskeleton and undergo conformational switching from a low-affinity "inactive" to a high-affinity "active" state. In the active conformation integrins enhance cell signalling and inappropriate integrin activation is linked to several pathologies including inflammation and cancer[1]. Hence, understanding integrin activity regulation is of major clinical relevance. Integrins are also crucial regulators of important processes in the brain such as neuronal cell migration, axonal outgrowth and synaptic plasticity[2] but the role of integrin activity regulation in these processes remains to be fully investigated.

Talin recruitment to the β-integrin tail triggers integrin activation and is regulated through the activity of the Rap1 GTPase and its effector Rap1-interacting adaptor molecule (RIAM)[3-5]. Integrin activity can be counterbalanced by integrin inactivating proteins such as SHARPIN, ICAP-1 and filamin[1,6,7], all of which interact with integrins and directly or indirectly interfere with talin-mediated integrin activation. However, potential mechanisms to block integrin activation at the level of Rap G-proteins remain unidentified.

SH3 and multiple ankyrin repeat domains (SHANK) 1-3 are a family of scaffold proteins found in the postsynaptic density (PSD) of excitatory synapses and are indispensable for normal brain function[8,9]. In addition, SHANK proteins are expressed in peripheral organs with largely unknown functions. Genetic alterations in *SHANK3* are responsible for a spectrum of neuropsychiatric disorders, including autism spectrum disorders (ASD), schizophrenia, intellectual disability and manic-like behaviour[10-16] and chromosomal deletions of the region containing *SHANK3* cause Phelan-McDermid syndrome (22q13 deletion syndrome) which manifests as neurological symptoms and affects many peripheral organs including the dermis, congruent with the wide tissue-distribution of SHANK3[17,18]. Recently, autism-like symptoms of *Shank3*-deficient mice were reversed by targeting actin regulators or Akt signalling[19,20] and adult restoration of *Shank3* in mice improved many of the autistic-like symptoms[21]. Thus, SHANK3 seems to actively contribute to signalling and the regulation of the cell cytoskeleton during and post development.

Results

SHANK1 and SHANK3 inhibit integrin activation

We previously performed a druggable genome-wide RNAi screen in 13 different human cell lines and analysed integrin activity using monoclonal anti-β1 integrin antibodies (9EG7 and 12G10) that specifically recognize the active receptor conformation[22]. Re-evaluation of these data revealed increased integrin activation (detected with either one or both of the antibodies) following *SHANK1* or *SHANK3* silencing in nine and in five out of the 13 cell lines tested, respectively (Fig. 1a). Although both SHANK1 and SHANK3 are major PSD scaffolding proteins in excitatory synapses, they are also widely expressed outside of the nervous system with currently unknown functions (publicly available GTEx portal data; Fig. 1b).

To validate a role for SHANK1 and SHANK3 in inhibiting integrin activation we employed a dual colour flow cytometric assay to measure cell-surface active integrins (based on the binding of a recombinant integrin ligand fragment, fibronectin [FN] repeats 7-10) relative to total cell-surface integrins in CHO cells[23,24]. Expression of rat Shank3-mRFP (Fig. 1c) or rat Shank1-GFP (Supplementary Fig. 1a) significantly reduced integrin activity, compared to mRFP or GFP alone (Fig. 1c and Supplementary Fig. 1a) without altering total β1-integrin surface levels. Moreover, the magnitude of Shank-mediated integrin inhibition was comparable to the effect of overexpressing SHARPIN-GFP (Fig. 1c), a known β1-integrin inhibitor in several cell types[7,25,26]. To confirm these findings we analysed integrin activity in the human HEK293 and MDA-MB-231 cell lines with opposing patterns of *SHANK3* and *SHANK1* expression (Supplementary Fig. 1b, 1c). Silencing of *SHANK3* in *SHANK3*–expressing HEK293 cells or *SHANK1* in *SHANK1*-expressing MDA-MB-231 cells (Supplementary Fig. 1d) triggered a significant increase in cell-surface active integrin levels (Fig. 1d,e and Supplementary Fig. 1e,f) without affecting total cell-surface receptor expression. *SHANK3*-silencing was nearly as efficient in activating β1-integrins as Mn^{2+} (Fig. 1d and Supplementary Fig. 1e) which binds to the integrin ectodomain and activates β1-integrin heterodimers via an outside-in mechanism[27]. Importantly, reintroduction of rat Shank3-mRFP or rat Shank1-GFP reversed the increased integrin activity in *SHANK3*- or *SHANK1*-silenced cells and reduced integrin activity levels in control-silenced cells (Fig. 1e and Supplementary Fig. 1f). Thus, the ability of *SHANK3*- and *SHANK1*-targeted siRNAs to increase β1-integrin activity was specifically due to the loss of each SHANK isoform rather than off-target effects.

To explore whether murine Shank3 regulates integrin activity as well, we isolated mouse mammary epithelial cells (MMECs), known to express Shank3[28] (Supplementary Fig. 1g), and mouse mammary fibroblasts (MMFs) lacking Shank3 (Supplementary Fig. 1g), from WT *Shank3αβ*$^{+/+}$ and *Shank3αβ*$^{-/-}$ mutant mice (specifically lacking the long α (containing SPN, Ank and SH3 domains) and β (containing Ank and SH3 domains) isoforms of SHANK3)[29,30] We observed markedly higher active integrin levels in MMECs, but not MMFs, isolated from *Shank3αβ*$^{-/-}$ compared to WT mice (*Shank3αβ*$^{+/+}$) (Fig. 1f and Supplementary Fig. 1h,i). Taken together, these data indicate that SHANK1 and SHANK3 function as inhibitors of β1-integrin activation.

SHANK1 and SHANK3 localize to membrane ruffles with inactive integrins

Next we investigated the subcellular localization of SHANKs in cells. In the absence of suitable reagents to detect endogenous SHANKs with immunofluorescence we expressed Shank3-mRFP (Fig. 1g; Supplementary figure 1j,k) or Shank1-GFP in MDA-MB-231 cells (Supplementary Fig. 1j). Both SHANK proteins localized to the periphery of the cell in actin-rich membrane ruffles positive for the membrane marker CAAX-GFP and the inactive integrin receptor (Fig. 1g and Supplementary Fig. 1j) as well as to the nucleus (the possible nuclear function of SHANKs was not investigated here further). Conversely, no co-localisation was observed between SHANKs and ECM-bound active integrins (Supplementary Fig. 1k). Membrane recruitment of SHANK3 was validated further with biochemical membrane fractionation, demonstrating SHANK3 in both the cytoplasmic and plasma membrane fractions (Fig. 1h), and with live-cell imaging showing dynamic localization of Shank3-mRFP to folding membrane areas (Fig. 1i and Supplementary video 1). Thus, SHANK1 and SHANK3 appear to predominantly localize to unattached membrane ruffles together with inactive integrin and actin.

SHANK1 and SHANK3 inhibit cell adhesion and spreading

Consistent with increased integrin activation (Fig. 1), *SHANK3* silencing in HEK293 cells or *SHANK1* silencing in MDA-MB-231 cells promoted cell adhesion to a fibronectin-collagen matrix over time as measured with the xCELLigence apparatus (Fig. 2a and Supplementary Fig. 2a). In addition, *SHANK3*-silenced HEK293 cells generated significantly more, yet smaller, adhesions (Fig. 2b-2e). Interestingly, *SHANK3* silencing also appeared to affect cell spreading. Downregulation of either SHANK isoform was sufficient to trigger a significant increase in cell area on the fibronectin-collagen-coated surface at 20 and 60 min post plating

compared to control-silenced cells (Fig. 2f,g and Supplementary Fig. 2b,c). Enhanced cell spreading was even more evident in cells plated on spatially restricted micropattern lines where *SHANK3* silencing resulted in significantly longer cell lengths compared to the control (Fig. 2h,i). Thus, SHANK1 and SHANK3 negatively regulate integrin-mediated adhesion and spreading in cells.

SHANK-mediated integrin inhibition is SHARPIN independent

We next sought to explore how SHANKs regulate integrin activity. SHARPIN binds to the ARR domain of SHANKs[31,32]. To determine whether SHANK-mediated integrin inactivation is SHARPIN dependent, we expressed SHARPIN- or Shank1-GFP in mouse embryonic fibroblasts (MEFs) generated from WT or SHARPIN-null (*cpdm*) animals[7] and measured surface levels of active (FN 7-10 binding), relative to total, β1-integrin. As expected, expression of both SHARPIN-GFP and Shank1-GFP reduced β1-integrin activation in WT MEFs (Supplementary Fig. 2d). Interestingly, Shank1-GFP expression decreased β1-integrin activation in *cpdm* MEFs to approximately the same extent as in WT MEFs (Supplementary Fig. 2d) suggesting that SHARPIN is dispensable for SHANK-mediated integrin inactivation.

Autism-linked mutations in *SHANK3* impair its integrin inhibitory function

The N-terminal SPN domain of SHANK1 and SHANK3 (Fig. 3a) is highly conserved[32] and missense mutations in the SPN domain of *SHANK3* (R12C and L68P) have been detected in patients with autism[33,34], highlighting the importance of the SPN domain for the proper function of SHANK3. In line with this notion, we found that expression of SHANK mutants (Shank3R12C or Shank3L68P) harbouring the identified ASD mutations[32] in *SHANK3*-silenced cells failed to rescue the increase in integrin activation triggered by loss of *SHANK3* (Fig. 3b). In contrast, re-expression of SHANK3 WT in the same cells completely restored integrin activity back to control levels (Fig. 3b). Furthermore, overexpression of the SPN-domain alone (SPN WT) was sufficient to significantly inhibit integrin activity in CHO cells (Fig. 3c). The L68P mutation significantly, and the RC12 mutation partially, impaired SPN-domain mediated integrin inhibition (Fig. 3c). An intact SPN domain was also critical for the ability of SHANK3 to regulate cell adhesion (Fig. 3d) and cell spreading (Fig. 3e). Unlike SHANK3 WT, SHANK3L68P failed to rescue *SHANK3*-silencing-induced effects on these processes. Thus, an intact SPN domain is a prerequisite for SHANK-dependent inhibition of integrin activity and the L68P mutation is more disruptive to SPN-domain activity than the R12C mutation.

Given the apparent functional importance of the ASD-associated SHANK3 mutations in integrin activity regulation, we investigated the effects of SHANK3 WT and L68P mutant in neurons. Overexpression of SHANK3 WT, but not the L68P mutant, in *Shank3αβ*$^{-/-}$ cortical neurons plated on laminin, inhibited β1-integrin activity in neuronal growth cones, structures regulated by integrins and integrin down-stream signalling[35,36] (Fig. 3f,g). In addition, expression of the SPN WT, but not the SPNL68P, inhibited integrin activity in growth cones of differentiating neuroblastoma cells on laminin (Supplementary Fig. 3a,b). Thus, SHANK3 inhibits β1-integrins also in neuronal cells.

Three-dimensional structure of the SHANK SPN-ARR region

To gain further insight into the role of the SHANK SPN domain in regulating integrin activity we determined the structure of the SPN-ARR region (the SPN domain is likely to form a compact unit with the adjacent ARR domain through intramolecular interactions[32]) by crystalizing the N-terminal fragment of SHANK3 (residues 1-348) and solving the structure by molecular replacement using two repeats from the core ankyrin domain of the crystal structure of human ankyrin-R (PDB: 1N11) as a template. The resulting structure, containing only 1 chain in the asymmetric unit and comprising residues 2-347 of SHANK3, was refined to 2.2Å; no electron density was detected for residues 1 and 348. Data collection and refinement statistics are given in Supplementary Table 1.

The structure of the SPN-ARR fragment demonstrated two distinct domains separated by a 19-residue linker with a well-defined conformation (Fig. 3h). The C-terminal ARR domain (residues 113-337) consists of seven canonical helix-turn-helix-β-hairpin/loop ankyrin repeats arranged in a curved solenoid structure. The loop region of each repeat forms a β-hairpin extending at 90^{o}-angle from the helices towards the centre of the solenoid, typical for ARR domains [37]. The β-hairpins of the repeats form a continuous flat surface that covers one end of the solenoid structure. The SPN domain (residues 8-93) positioned on top of the ARR β-hairpin surface has a ubiquitin-like fold (Ubl) closely resembling the Ubl within the talin F0 domain[38,39] (Fig. 3i and Supplementary Fig. 3c). The SPN domain makes charged and polar contacts with the outer surface of the β-hairpins of repeats 2 and 3 (Fig. 3j). The N-terminal part of the linker region connecting the SPN and ARR domains runs along the ARR β-hairpin surface, making a range of polar contacts (Fig. 3j). The C-terminal region of the linker folds into a 2-turn α-helix that packs against the outer end of the ankyrin repeat 1.

NMR-studies confirmed that the SPN-ARR region of SHANKs exist as an integrated unit in solution (see Supplementary Fig. 3d for the data and a detailed description).

Structure of SHANK3 SPN-ARR reveals a previously uncharacterized Ras/Rap-association (RA) domain

The similarity between the SHANK SPN and talin F0 structures, and the reported interaction between talin F0 and Rap1[39,40], prompted us to investigate whether SHANK SPN is an RA domain interacting with Ras and Rap GTPases. Sequence alignment of SHANK1 and SHANK3 SPN domains with the well-characterized RA domains of RalGDS, Raf and Byr revealed the presence of consensus Ras/Rap-recognizing positive charges (residues R12 and K22) in the β1 and β2 strands of both SHANK1 and SHANK3 isoforms and a distinctive distribution of hydrophobic residues in the same region that are typically associated with RA domains[41] (Fig. 4a). Furthermore, the Ras/Rap recognition side-chains of the SPN and RalGDS RA domains are well aligned in space (Fig. 4b). The only deviation from the consensus is the substitution of a positive charge, corresponding to position 52 in RalGDS, with an alanine in SHANK1 and SHANK3. However, other exposed positive charges (R38 or R25) in the vicinity of R12 and K22 may compensate for the missing charge in the α1-helix of the SHANK proteins (Fig. 4b,c). These data strongly suggest that SHANK SPN belongs to the RA family of Ubl domains.

The SHANK SPN domain is a functional RA domain as it coimmunoprecipitated with WT and constitutively active (G12V mutant) forms of H-Ras but not with the dominant negative H-Ras S17N variant (Fig. 4d). Thus, SHANK3 preferentially binds to the GTP-bound, active H-Ras. Additionally we found that the SHANK3 SPN domain interacts with several Ras and Rap proteins in their constitutively active and WT forms (Fig. 4e). However, in line with the notion that RA domains are promiscuous in terms of binding to several different Ras family members, but not Rho G-proteins, SHANK3 SPN did not interact with Rac1-GTP or Cdc42-GTP (Supplementary Fig. 4a).

Autism-associated mutations in SHANK3 SPN impair Ras and Rap binding

Next we predicted the potential effects of ASD-related mutations by superimposing the SHANK3 SPN structure on the RalGDS RA domain in complex with Ras (PDB ID 1LFD). The model demonstrated that most of the key ion-pair and polar interactions at the interface are preserved in SHANK3. In this model the position of the SHANK3 SPN R12 side-chain is optimal for forming an ion-pair with E37 of Ras (Fig. 4f). Thus, the R12C mutation identified

in ASD is expected to significantly reduce Ras binding. The second ASD mutation in the SPN domain, L68P, affects one of the key residues of the hydrophobic core (Fig. 3a) and is expected to disrupt the SPN fold, potentially causing loss of Ras interaction. As predicted from these structural analyses, the R12C and L68P ASD mutations within the SPN domain disrupted SHANK3 SPN domain interaction with active (G12V mutant) Ras as well as Rap1 variants (Fig. 4g,h), even though SPN R12C retained partial binding to Rap1b in pull-downs (Fig. 4g,h).

Accordingly, isothermal titration calorimetry (ITC) measurements with purified recombinant proteins indicated a very strong interaction between SHANK3 SPN-ARR and Rap1b-GTP (Kd = 0.2 ± 0.05 μM) (Fig. 4i). In comparison the Kd for SPNR12C binding to Rap1b was 2.2 ± 0.26 μM, indicating a 10-fold reduction in affinity towards Rap1b (Fig. 4j), in line with the immunoprecipitation and modelling data. The interaction between WT SPN with H-Ras-GTP was weaker (Kd = 3.3 ± 0.14 μM) (Supplementary Fig. 4b) and further reduced in the presence of the R12C mutation, and no interaction was observed with H-Ras-GDP (Supplementary Fig. 4c-e). The interaction between SHANK1 and H-Ras-GTP, although weaker (Kd = 5.9 ± 0.73 μM), was within the range of affinities determined for RA domains (Supplementary Fig. 4f)[41]. The enthalpy of SHANK3 SPN interaction with Rap1-GTP was significantly lower than that observed with H-Ras-GTP (Supplementary Fig. 4g), suggesting stronger ion-pair interactions or formation of additional hydrogen bonds at the interface between the SHANK SPN domain and Rap1-GTP. We could not ascertain the effect of the ASD-related L68P mutation in ITC experiments as we were unable to produce soluble mutant protein. However, this insolubility may point towards a role for L68 in the folding of the SPN domain. Taken together these data indicate that the SPN domain of SHANK interacts with Ras and Rap in a manner similar to other RA domain-containing proteins and that the primary effect of ASD mutations is a loss of interaction with small G-proteins.

SHANK3 interferes with integrin activation by sequestering Rap1a and R-Ras

Active small GTPases Rap1 [4, 42-45] and R-Ras [46-48] activate integrins via inside-out signalling. To explore whether β1-integrin inhibition by SHANK3 is Rap1- and R-Ras-dependent we performed the flow cytometric-based integrin activity assays in HEK293 cells. Expression of a constitutively active Rap1a (Rap1Q63E) or constitutively active R-Ras (R-RasG38V) enhanced integrin activity (Fig. 5a and Supplementary Fig. 5a). Co-expression of Shank3-mRFP inhibited the ability of both Rap1Q63E and R-RasG38V to augment β1-integrin activity which was comparable to control levels (Fig. 5a and Supplementary Fig. 5a). The

ability of Mn^{2+} to induce integrin outside-in activation is dependent on active Rap1 availability in cells[49]. Accordingly, we find that Mn^{2+}-induced integrin activity is significantly impaired in Shank3-mRFP overexpressing CHO cells (Supplementary Fig. 5b). Active Rap1a-induced integrin activation promotes marked cell spreading and flattening[50]. Consistent with the ability of SHANK3 to attenuate Rap1-dependent integrin activation, co-expression of SHANK3 with Rap1 fully reversed the cell spreading phenotype (Fig. 5b and 5c). Notably, the Rap-binding defective Shank3L68P and Shank3R12C mutants failed to counteract Rap1Q63E- or R-RasG38V-mediated integrin activation (Fig. 5a and Supplementary Fig. 5a). In hippocampal neurons integrin ligands stimulate [51] and SHANK3 overexpression suppresses [52] the formation of new filopodia. We found that overexpression of Shank3 WT-GFP, but not the L68P mutant, inhibits filopodia number in MAP2-positive rat hippocampal neurites (Fig. 5d and 5e). Furthermore, WT SPN-GFP overexpression reduced filopodia number in neurites of differentiating neuroblastoma cells in comparison to GFP (Fig. 5f, g). However, the number of neurites in addition to neurite length and branching were not significantly affected by SHANK3 WT or L68P overexpression (Supplementary Fig. 5c), in agreement with the normal brain architecture reported for most Shank3-deficient mouse models[53]. Importantly, pharmacological inhibition of Rap1[54,55] reverted integrin activity (Fig. 5h) and cell spreading (Fig. 5i,j) in *SHANK3*-silenced cells back to control levels, suggesting that SHANK3 regulates integrin activity and cell spreading in a Rap1-dependent manner. These data suggest that SHANK3 antagonizes Rap1a- and R-Ras-induced integrin activation and signalling.

Rap1-GTP targeting to the plasma membrane is essential for RIAM recruitment and talin-mediated integrin activation[4]. In line with the ability of SHANK3 to counteract active Rap1-dependent signalling in cells, we found significant colocalization between Shank3-mRFP and Rap1Q63E-GFP especially in membrane ruffles of cells (Fig. 6a). In addition, *SHANK3* silencing in cells markedly increased Rap1 levels in the plasma membrane fraction (Fig. 6b) and triggered a marked enrichment of active Rap1 (Raichu-Rap1 fluorescence resonance energy transfer (FRET) probe [56]) at the cell periphery close to the plasma membrane compared to a more uniform distribution of active Rap1 in control cells (Fig. 6c-e). This was due to altered Rap1 localization in cells as total Rap1-GTP levels in cells were not significantly altered upon *SHANK3* silencing (Supplementary Fig. 6). Thus, SHANK expression appears to regulate the bioavailability of active Rap1 particularly on the plasma membrane.

SHANKs reduce integrin-talin complexes and regulate adhesion dynamics in cells

Interestingly, using the proximity ligation assay (PLA), we observed that *SHANK3* silencing also promotes talin recruitment to β1-integrin (Fig. 7a,b). Furthermore, endogenous talin co-immunoprecipitated with β1-integrin more efficiently in *SHANK3*-silenced cells (Fig. 7c; 2.1 ± 0.7 fold increase, n = 3). Live-cell imaging revealed that depletion of *SHANK1* significantly enhanced talin recruitment to newly forming membrane protrusions in MDA-MB-231 cells (Fig. 7d,e and Supplementary Video 2). In addition, *SHANK1* silencing reduced the lifetime of paxillin-positive focal adhesions (Fig. 7f,g), corroborating our data from fixed cells displaying more small adhesions and faster cell spreading. Altogether, these data suggest that SHANK-mediated segregation of Rap1 away from the plasma membrane affects talin recruitment to integrin tails and thus impedes integrin activation. However, whether SHANKs directly affect Rap1/RIAM/talin complex formation remains to be investigated.

SHANK3 attenuates cell migration and invasion

Increased integrin activity is implicated in altered cell migration as well as enhanced cancer cell invasion and metastasis[7,57,58]. To assess the role of SHANKs in cell migration we analysed random motility of *SHANK*-silenced cells in 2D. Time-lapse imaging revealed that depletion of *SHANK3* in HEK293 cells or *SHANK1* in MDA-MB-231 cells promotes a significant increase in migration velocity and a converse decrease in directionality of migration (Fig. 8a-c, Supplementary Fig. 7a-c). The effect of SHANK1 silencing on migration was fully reversed upon re-expression of Shank1-GFP (Fig. 8d-e). Previous work has linked increased random motility in 2D to enhanced cancer cell invasion in 3D[59]. In line with this notion we observed that *SHANK1* silencing significantly promoted cell invasion into collagen hydrogels (Fig. 8f,g). Thus, increased integrin activity in *SHANK*-silenced cells promotes cell spreading, random migration and 3D invasion demonstrating that SHANKs are biologically important regulators of integrin function.

Discussion

Regulation of integrin activity is of central importance to human health[1]. The critical role of Rap1 in the final steps of integrin activation is well-established[5]; active Rap1 recruits RIAM and talin to the plasma membrane to facilitate integrin activation. However, mechanisms to fine-tune this activation or to antagonize it are not fully understood. Here we describe that scaffold proteins SHANK1 and SHANK3 act as negative regulators of integrin activity in several cell types and consequently interfere with cell adhesion, spreading, migration and invasion (Fig. 8h), and with filopodia formation in neurites. Furthermore, we demonstrate that ASD-linked SHANK3 mutants are functionally deficient in binding to active Ras family members Rap1 and R-Ras and in mediating integrin inhibition.

The crystal structure of the SHANK3 N-terminal SPN-ARR region confirmed the intramolecular interaction between both domains detected previously[32]. More importantly, it allowed us to elucidate the molecular mechanism by which SHANKs regulate integrin activity: (1) the SPN is an RA domain most similar to the N-terminal F0 motif of talin; (2) the SHANK SPN domain binds active, GTP-bound forms of H-Ras, Rap1 and other Ras subfamily members with high affinity; (3) ASD-related mutations in residues R12 and L68 in the SHANK3 SPN domain impair binding to Ras proteins and the ability to antagonize β1-integrin activity in cells. Thus, the primary mechanism of SHANK-dependent integrin antagonism most likely stems from the ability to interfere with Rap1 or R-Ras effector binding through direct competition (Fig. 8h). It is important to note that, unlike the specific integrins expressed on leukocytes or platelets, Rap1 is not absolutely essential for β1-integrin activation and a significant pool of β1-integrin remains active in adherent cells even once Rap1 is inhibited[1,7]. Thus, several pathways, in addition to the Rap1-RIAM-talin axis, are likely to be involved in the spatio-temporal fine-tuning of β1-integrin activity in adherent cells at any given time.

ECM ligands and specific adhesion receptors such as integrins are also important in the central nervous system, in dendritic spines and synapses[60]. Autism-like deficits of Shank3-deficient mice can be rescued by targeting the actin regulators Rac and cofilin[20], by re-expressing *Shank3* in adult mice[21] or by inhibiting Akt signalling[19]. Given the ability of integrins to regulate all of these proteins, our identification of a potential role for SHANK proteins in regulating integrin activity in neuronal growth cones is most likely relevant to the neurodevelopmental disorder of these mice.

Our observation that SHANKs antagonize integrin activation, by limiting active Rap1 bioavailability on the plasma membrane, provides a significant advance to our understanding of integrin activity regulation. However, SHANK3-mediated control of Ras and Rap may contribute to integrin-independent pathways as well. SHANK3 is a major scaffold proteins within the PSD of dendritic spines[61]. Ras activation promotes spine growth, while Rap1 induces spine shrinkage[62]. Thus, sequestration of the activated forms of G-proteins may contribute to maintaining the balance between Ras and Rap1 activities given that the R12C mutation compromises the effect of SHANK3 overexpression on spine size and synaptic transmission[52,63]. Furthermore, the ability of SHANK1 and SHANK3 to sequester active Ras- and Rap-family members is likely to be important in other biological contexts including Ras-driven human carcinomas.

References

1. Bouvard, D., Pouwels, J., De Franceschi, N. & Ivaska, J. Integrin inactivators: balancing cellular functions in vitro and in vivo. *Nature reviews. Molecular cell biology* **14**, 430-442 (2013).

2. Levy, A.D., Omar, M.H. & Koleske, A.J. Extracellular matrix control of dendritic spine and synapse structure and plasticity in adulthood. *Frontiers in neuroanatomy* **8**, 116 (2014).

3. Lafuente, E.M. *et al.* RIAM, an Ena/VASP and Profilin ligand, interacts with Rap1-GTP and mediates Rap1-induced adhesion. *Developmental cell* **7**, 585-595 (2004).

4. Lee, H.S., Lim, C.J., Puzon-McLaughlin, W., Shattil, S.J. & Ginsberg, M.H. RIAM activates integrins by linking talin to ras GTPase membrane-targeting sequences. *The Journal of biological chemistry* **284**, 5119-5127 (2009).

5. Calderwood, D.A., Campbell, I.D. & Critchley, D.R. Talins and kindlins: partners in integrin-mediated adhesion. *Nature reviews. Molecular cell biology* **14**, 503-517 (2013).

6. Liu, J. *et al.* Structural mechanism of integrin inactivation by filamin. *Nature structural & molecular biology* **22**, 383-389 (2015).

7. Rantala, J.K. *et al.* SHARPIN is an endogenous inhibitor of beta1-integrin activation. *Nature cell biology* **13**, 1315-1324 (2011).

8. Kreienkamp, H.J. Scaffolding proteins at the postsynaptic density: shank as the architectural framework. *Handbook of experimental pharmacology*, 365-380 (2008).

9. Sheng, M. & Kim, E. The Shank family of scaffold proteins. *Journal of cell science* **113 (Pt 11)**, 1851-1856 (2000).

10. Betancur, C. & Buxbaum, J.D. SHANK3 haploinsufficiency: a "common" but underdiagnosed highly penetrant monogenic cause of autism spectrum disorders. *Molecular autism* **4**, 17 (2013).

11. Carbonetto, S. A blueprint for research on Shankopathies: a view from research on autism spectrum disorder. *Developmental neurobiology* **74**, 85-112 (2014).

12. Gauthier, J. *et al.* De novo mutations in the gene encoding the synaptic scaffolding protein SHANK3 in patients ascertained for schizophrenia. *Proceedings of the National Academy of Sciences of the United States of America* **107**, 7863-7868 (2010).

13. Grabrucker, S. *et al.* The PSD protein ProSAP2/Shank3 displays synapto-nuclear shuttling which is deregulated in a schizophrenia-associated mutation. *Experimental neurology* **253**, 126-137 (2014).

14. Guilmatre, A., Huguet, G., Delorme, R. & Bourgeron, T. The emerging role of SHANK genes in neuropsychiatric disorders. *Developmental neurobiology* **74**, 113-122 (2014).

15. Han, K. *et al.* SHANK3 overexpression causes manic-like behaviour with unique pharmacogenetic properties. *Nature* **503**, 72-77 (2013).

16. Leblond, C.S. *et al.* Meta-analysis of SHANK Mutations in Autism Spectrum Disorders: a gradient of severity in cognitive impairments. *PLoS genetics* **10**, e1004580 (2014).

17. Phelan, K. & McDermid, H.E. The 22q13.3 Deletion Syndrome (Phelan-McDermid Syndrome). *Molecular syndromology* **2**, 186-201 (2012).

18. Sarasua, S.M. *et al.* Clinical and genomic evaluation of 201 patients with Phelan-McDermid syndrome. *Human genetics* **133**, 847-859 (2014).

19. Bidinosti, M. *et al.* CLK2 inhibition ameliorates autistic features associated with SHANK3 deficiency. *Science* **351**, 1199-1203 (2016).

20. Duffney, L.J. *et al.* Autism-like Deficits in Shank3-Deficient Mice Are Rescued by Targeting Actin Regulators. *Cell reports* **11**, 1400-1413 (2015).

21. Mei, Y. *et al.* Adult restoration of Shank3 expression rescues selective autistic-like phenotypes. *Nature* **530**, 481-484 (2016).

22. Pellinen, T. *et al.* A functional genetic screen reveals new regulators of beta1-integrin activity. *Journal of cell science* **125**, 649-661 (2012).

23. Bouaouina, M., Harburger, D.S. & Calderwood, D.A. Talin and signaling through integrins. *Methods in molecular biology* **757**, 325-347 (2012).

24. Harburger, D.S., Bouaouina, M. & Calderwood, D.A. Kindlin-1 and -2 directly bind the C-terminal region of beta integrin cytoplasmic tails and exert integrin-specific activation effects. *The Journal of biological chemistry* **284**, 11485-11497 (2009).

25. De Franceschi, N. *et al.* Mutually Exclusive Roles of SHARPIN in Integrin Inactivation and NF-kappaB Signaling. *PloS one* **10**, e0143423 (2015).

26. Pouwels, J. *et al.* SHARPIN regulates uropod detachment in migrating lymphocytes. *Cell reports* **5**, 619-628 (2013).

27. Elices, M.J., Urry, L.A. & Hemler, M.E. Receptor functions for the integrin VLA-3: fibronectin, collagen, and laminin binding are differentially influenced by Arg-Gly-Asp peptide and by divalent cations. *The Journal of cell biology* **112**, 169-181 (1991).

28. Schuetz, G. *et al.* The neuronal scaffold protein Shank3 mediates signaling and biological function of the receptor tyrosine kinase Ret in epithelial cells. *The Journal of cell biology* **167**, 945-952 (2004).

29. Schmeisser, M.J. *et al.* Autistic-like behaviours and hyperactivity in mice lacking ProSAP1/Shank2. *Nature* **486**, 256-260 (2012).

30. Wang, X., Xu, Q., Bey, A.L., Lee, Y. & Jiang, Y.H. Transcriptional and functional complexity of Shank3 provides a molecular framework to understand the phenotypic heterogeneity of SHANK3 causing autism and Shank3 mutant mice. *Molecular autism* **5**, 30 (2014).

31. Lim, S. *et al.* Sharpin, a novel postsynaptic density protein that directly interacts with the shank family of proteins. *Molecular and cellular neurosciences* **17**, 385-397 (2001).

32. Mameza, M.G. *et al.* SHANK3 gene mutations associated with autism facilitate ligand binding to the Shank3 ankyrin repeat region. *The Journal of biological chemistry* **288**, 26697-26708 (2013).

33. Durand, C.M. *et al.* Mutations in the gene encoding the synaptic scaffolding protein SHANK3 are associated with autism spectrum disorders. *Nature genetics* **39**, 25-27 (2007).

34. Gauthier, J. *et al.* Novel de novo SHANK3 mutation in autistic patients. *American journal of medical genetics. Part B, Neuropsychiatric genetics : the official publication of the International Society of Psychiatric Genetics* **150B**, 421-424 (2009).

35. Myers, J.P. & Gomez, T.M. Focal adhesion kinase promotes integrin adhesion dynamics necessary for chemotropic turning of nerve growth cones. *The Journal of neuroscience : the official journal of the Society for Neuroscience* **31**, 13585-13595 (2011).

36. Plantman, S. *et al.* Integrin-laminin interactions controlling neurite outgrowth from adult DRG neurons in vitro. *Molecular and cellular neurosciences* **39**, 50-62 (2008).

37. Mosavi, L.K., Cammett, T.J., Desrosiers, D.C. & Peng, Z.Y. The ankyrin repeat as molecular architecture for protein recognition. *Protein science : a publication of the Protein Society* **13**, 1435-1448 (2004).

38. Elliott, P.R. *et al.* The Structure of the talin head reveals a novel extended conformation of the FERM domain. *Structure* **18**, 1289-1299 (2010).

39. Goult, B.T. *et al.* Structure of a double ubiquitin-like domain in the talin head: a role in integrin activation. *The EMBO journal* **29**, 1069-1080 (2010).

40. Plak, K., Pots, H., Van Haastert, P.J. & Kortholt, A. Direct Interaction between TalinB and Rap1 is necessary for adhesion of Dictyostelium cells. *BMC Cell Biol* **17**, 1 (2016).

41. Wohlgemuth, S. *et al.* Recognizing and defining true Ras binding domains I: biochemical analysis. *Journal of molecular biology* **348**, 741-758 (2005).

42. Reedquist, K.A. *et al.* The small GTPase, Rap1, mediates CD31-induced integrin adhesion. *The Journal of cell biology* **148**, 1151-1158 (2000).

43. Posern, G., Weber, C.K., Rapp, U.R. & Feller, S.M. Activity of Rap1 is regulated by bombesin, cell adhesion, and cell density in NIH3T3 fibroblasts. *The Journal of biological chemistry* **273**, 24297-24300 (1998).

44. Tsukamoto, N., Hattori, M., Yang, H., Bos, J.L. & Minato, N. Rap1 GTPase-activating protein SPA-1 negatively regulates cell adhesion. *The Journal of biological chemistry* **274**, 18463-18469 (1999).

45. Katagiri, K. *et al.* Rap1 is a potent activation signal for leukocyte function-associated antigen 1 distinct from protein kinase C and phosphatidylinositol-3-OH kinase. *Molecular and cellular biology* **20**, 1956-1969 (2000).

46. Zhang, Z., Vuori, K., Wang, H., Reed, J.C. & Ruoslahti, E. Integrin activation by R-ras. *Cell* **85**, 61-69 (1996).

47. Lehto, M. *et al.* The R-Ras interaction partner ORP3 regulates cell adhesion. *Journal of cell science* **121**, 695-705 (2008).

48. Weber-Boyvat, M. *et al.* OSBP-related protein 3 (ORP3) coupling with VAMP-associated protein A regulates R-Ras activity. *Experimental cell research* **331**, 278-291 (2015).

49. de Bruyn, K.M., Rangarajan, S., Reedquist, K.A., Figdor, C.G. & Bos, J.L. The small GTPase Rap1 is required for Mn(2+)- and antibody-induced LFA-1- and VLA-4-mediated cell adhesion. *The Journal of biological chemistry* **277**, 29468-29476 (2002).

50. Arthur, W.T., Quilliam, L.A. & Cooper, J.A. Rap1 promotes cell spreading by localizing Rac guanine nucleotide exchange factors. *The Journal of cell biology* **167**, 111-122 (2004).

51. Shi, Y. & Ethell, I.M. Integrins control dendritic spine plasticity in hippocampal neurons through NMDA receptor and Ca2+/calmodulin-dependent protein kinase II-mediated actin reorganization. *The Journal of neuroscience : the official journal of the Society for Neuroscience* **26**, 1813-1822 (2006).

52. Durand, C.M. *et al.* SHANK3 mutations identified in autism lead to modification of dendritic spine morphology via an actin-dependent mechanism. *Molecular psychiatry* **17**, 71-84 (2012).

53. Wang, X. *et al.* Synaptic dysfunction and abnormal behaviors in mice lacking major isoforms of Shank3. *Human molecular genetics* **20**, 3093-3108 (2011).

54. McSherry, E.A., Brennan, K., Hudson, L., Hill, A.D. & Hopkins, A.M. Breast cancer cell migration is regulated through junctional adhesion molecule-A-mediated activation of Rap1 GTPase. *Breast cancer research : BCR* **13**, R31 (2011).

55. Muramatsu, R. *et al.* RGMa modulates T cell responses and is involved in autoimmune encephalomyelitis. *Nature medicine* **17**, 488-494 (2011).

56. Ohba, Y., Kurokawa, K. & Matsuda, M. Mechanism of the spatio-temporal regulation of Ras and Rap1. *The EMBO journal* **22**, 859-869 (2003).

57. Jin, J.K. *et al.* Talin1 phosphorylation activates beta1 integrins: a novel mechanism to promote prostate cancer bone metastasis. *Oncogene* **34**, 1811-1821 (2015).

58. Felding-Habermann, B. *et al.* Integrin activation controls metastasis in human breast cancer. *Proceedings of the National Academy of Sciences of the United States of America* **98**, 1853-1858 (2001).

59. Caswell, P.T. *et al.* Rab-coupling protein coordinates recycling of alpha5beta1 integrin and EGFR1 to promote cell migration in 3D microenvironments. *The Journal of cell biology* **183**, 143-155 (2008).

60. Koleske, A.J. Molecular mechanisms of dendrite stability. *Nature reviews. Neuroscience* **14**, 536-550 (2013).

61. Baron, M.K. *et al.* An architectural framework that may lie at the core of the postsynaptic density. *Science* **311**, 531-535 (2006).

62. Lee, K.J. *et al.* Requirement for Plk2 in orchestrated ras and rap signaling, homeostatic structural plasticity, and memory. *Neuron* **69**, 957-973 (2011).

63. Arons, M.H. *et al.* Autism-associated mutations in ProSAP2/Shank3 impair synaptic transmission and neurexin-neuroligin-mediated transsynaptic signaling. *The Journal of neuroscience : the official journal of the Society for Neuroscience* **32**, 14966-14978 (2012).

Acknowledgements

We thank J. Jukkala, P. Laasola, J. Siivonen, H-H. Hönck and V. Kolbe for technical assistance, M. Saari for help with the microscopes; C. Guzman for image and statistical analysis; G. Rosenberger for HA-tagged G-protein expression constructs; M. Matsuda for the Raichu-Rap1 probe; A. Shcheglovitov for pHAGE-EGFP-Shank3 construct and Cell Imaging Core facility, University of Turku Centre for Biotechnology for help with imaging. This study has been supported by the Academy of Finland (J.I., J.P., E.P.), ERC Starting Grant, ERC Consolidator Grant (615258), the Sigrid Juselius Foundation, the Finnish Cancer Organization (J.I.) and Deutsche Forschungsgemeinschaft (GRK1459; to H.-J.K.). J.L. is supported by Turku Doctoral Programme of Molecular Medicine (TuDMM). T.Z. was supported by the Biotechnology and Biological Sciences Research Council (BBSRC) DTP fellowship. M.G and G.J. are supported by an EMBO Long-Term Fellowship. F.H.N. is supported by DAAD; V.M. is supported by Dr. Hans Ritz und Lieselotte Ritz Stiftung. We thank umif (Hamburg) for access to microscopes. The X-ray data were collected at Diamond Light Source (UK) under Liverpool BAG allocation.

Author contributions

Conceptualization, J.I., H-J.K. and I.B.; Methodology, J.L., G.J., T.Z. and M.G., Formal Analysis, T.Z., G.J., I.B. and J.L.; Investigation, J.L., T.Z. M.G., G.J., N.dF. E.P. M.B., V.M., F.HN., J.I., H-J.K. and I.B. Resources, T.B, J.I., H-J.K. and I.B.; Writing-Original Draft, J.I., H-J.K. I.B. and M.G.; Writing-Reviewing , J.I., J.L., M.G., G.J., H-J.K., H.H., and I.B.; Visualization, G.J., J.L., M.G., I.B., H.H., and H-J.K. Supervision, J.P., J.I., H-J.K. and I.B.; Funding Acquisition, J.I., H-J.K. and I.B.

Figure Legends

Figure 1 | SHANK1 and SHANK3 inhibit β1-integrin activation

a, Hierarchical clustering of β1-integrin activity (9EG7 and/or 12G10 antibodies; red: increased and blue: decreased compared to control-silenced cells (Z-score)) in 13 human cell lines upon *SHANK1* or *SHANK3* silencing with two independent siRNAs (#1 or #2). Results taken from a high-density cell-spot microarray.

b, *SHANK3* gene expression (log_{10}RPKM: Reads Per Kilobase of transcript per Million mapped reads) in human tissues analysed using the publicly available GTEx portal (Grey region: brain tissues).

c-e, Flow cytometric (FACS) analysis of integrin activity in the indicated conditions. **c**, Quantification shows reduced active cell-surface integrin (FN 7-10 binding) relative to total cell-surface α5β1-integrin (PB1 antibody) in Shank3-mRFP- or Sharpin-GFP-expressing cells compared to mRFP/GFP cells. **d,** *SHANK3*-silencing triggers β1-integrin activation (active β1-integrin: 9EG7 antibody; total β1-integrin: P5D2) similarly to Mn^{2+}. **e**, Shank3-mRFP re-expression abrogates integrin activation induced by *SHANK3* silencing. Data represent mean ± SEM (n = 5 (c), 3 (d), 4 (e) independent experiments; 5000 (mRFP- or GFP-positive cells) or 10000 cells (*SHANK*3-silenced) per experiment).

f, FACS analysis (active β1-integrin: 9EG7 antibody; total β1-integrin: MAB1997) in MMECs isolated from *Shank3αβ*$^{-/-}$ mice compared to *Shank3αβ*$^{+/+}$ (mean of 2 independent experiments; cells pooled from three mice per experiment).

g, Shank3-mRFP-expressing MDA-MB-231 cells plated on fibronectin-collagen demonstrate SHANK3 localization with inactive β1-integrin (MAB13) and membrane marker CAAX-GFP in membrane ruffles. Shown is a representative confocal slice (middle plane). ROI: region of interest. Scale bar = 20 μm (original image) and 10 μm (ROI).

h, HEK293 subcellular fractions. Cyt: cytoplasmic; PM: plasma membrane; Na^+/K^+ pump: PM marker; tubulin: Cyt marker; 10 % Lys: 10 % of total lysate.

i, Shank3-mRFP-expressing MDA-MB-231 cells plated on fibronectin and imaged live using a spinning disk microscope (1 picture every 10 s). Scale bar = 20 μm (original image) and 5 μm (ROI).

Tukey box plots represent median and 25th and 75th percentiles (interquartile range); points displayed as outliers if 1.5 times above or below the interquartile range; outliers are represented by dots. Statistical analysis: Student's t-test. Statistics source data can be found in

Supplementary Table 3. Unprocessed original scans of blots are shown in Supplementary Fig 8.

Figure 2 | Loss of SHANK1 and SHANK3 promotes cell adhesion and spreading

a, Rate of cell adherence (cell index) of HEK293 cells monitored in real-time using the xCELLigence system shows enhanced cell attachment upon *SHANK3* silencing on a fibronectin-collagen substrate. BSA was used as a control for background binding. Data represent mean ± SEM (n = 4 independent experiments; average of 4 wells per experiment, 20000 cells/well).

b, Representative confocal images of control- and *SHANK3*-silenced HEK293 cells adhering to a fibronectin-collagen substrate for 15 min. Cells were stained for active β1-integrin (9EG7, green), paxillin (grey) and F-actin (phalloidin, red) to mark adhesions. Shown are confocal slices from the bottom surface. Scale bar = 10 μm (original image) and 5 μm (ROI).

c-e, Quantification of the active integrin (9EG7-positive) adhesions in b showing that *SHANK3*-silenced HEK293 cells form more (c) but smaller (d) adhesions as compared to control-silenced cells. The distribution of adhesion size is also shown (e). Adhesions were analysed using the Cell Profiler software. Data shown as Tukey box plots (n = 15 siCTRL cells and 22 siSHANK3 cells from 3 independent experiments).

f,g, Representative confocal images (f) and quantification (g) showing increased HEK293 cell spreading on a fibronectin-collagen substrate upon *SHANK3* silencing. Cells were stained for F-actin (phalloidin). Scale bar = 10 μm. Quantification of cell area at 20 or 60 min post-plating was analysed using Image J. Data displayed as Tukey box plots (n = 47 cells (20 min) or 72 cells (60 min) from 3 independent experiments).

h,**i**, Representative confocal images (h) and quantification (i) showing increased HEK293 cell length upon *SHANK3* silencing compared to control cells on fibronectin-collagen-coated micropattern lines at 20 or 60 min post-plating. Scale bar = 10 μm. Data are displayed as Tukey box plots (n = 29 cells (20 min) or 46 cells (60 min) from 3 independent experiments). Tukey box plots represent median and 25^{th} and 75^{th} percentiles (interquartile range); points displayed as outliers if 1.5 times above or below the interquartile range; outliers are represented by dots. Statistical analysis: Student's t-test. Statistics source data can be found in Supplementary Table 3.

Figure 3 | Structural analysis of the SHANK3 SPN-ARR region

a, Illustration of SHANK3 protein domains. SPN: Shank/ProSAP N-terminal domain; ARR: ankyrin repeat domain; SH3: Src homology 3 domain; PDZ: PSD-95/Discs large/ZO-1 domain; PP: proline-rich region; SAM: sterile alpha motif domain. ASD-related mutations (R12C, L68P) in the SPN domain are indicated.

b,c, FACS analysis of integrin activity. **b**, Re-expression of Shank3-mRFP L68P or R12C in *SHANK3*-silenced HEK293 cells has no effect on integrin activity. **c**, Expression of SPN WT-GFP alone inhibits integrin activity in CHO cells. Data represent mean ± SEM (n = 4 (b), 5 (c) independent experiments; 5000 mRFP or GFP-positive cells analysed per experiment). Bars shown as dashed line are from Fig. 1e.

d,e, HEK293 cell adhesion and spreading monitored as in 2a and 2g. Re-expression of WT Shank3-mRFP, but not L68P mutant, decreases cell adhesion (d) and spreading (20 min) (e) induced by *SHANK3* silencing. (d) Data represent mean ± SEM (*n* = 6 independent experiments; average of 4 wells per experiment, 20000 cells/well). (e) Tukey box plots are shown (n = 138, 224, 99, 101 cells from left to right) from 3 independent experiments.

f,g, Representative confocal images (f) and quantification (g) of integrin activity in *Shank3*$\alpha\beta^{-/-}$ mouse cortical neurons plated on laminin. Overexpression of SHANK3 WT, but not the L68P mutant, reduces active integrin (9EG7) in growth cones relative to area. Scale bar = 5 μm. Mean grey value (active integrin intensity) analysed with Image J software (g). Data represent mean ± SEM (*n* = 40 (WT) or 34 (L68P) growth cones from 3 independent experiments; cells pooled from 7-8 embryos per experiment).

h, Cartoon representation of the SPN-ARR crystal structure. The SPN domain is shown in cyan, linker region in orange and ARR domain in green. Side-chains of R12 and L68, mutated in ASD, are depicted as red sticks.

i, Superposition of SHANK3 SPN (cyan) and talin F0 (grey) domain structures.

j, Interface between SPN and ARR domains showing side-chains of the contacting residues as sticks. Polar oxygen atoms are highlighted in red and nitrogen in blue. Protein orientation was changed slightly relative to (h) to optimize side-chain representation.

Tukey box plots represent median and 25th and 75th percentiles (interquartile range); points displayed as outliers if 1.5 times above or below the interquartile range; outliers are represented by dots. Statistical analysis: Student's t-test. Statistics source data can be found in Supplementary Table 3.

Figure 4 | SHANK3 interaction with Ras and Rap

a, Alignment of SHANK1 (rat, Q9WV48) and SHANK3 (rat, Q9JLU4) protein sequences with the Ras/Rap recognition elements of known RA domains (Ra1GDS: rat, Q03386; C-Raf: human, P04049; Byr: yeast, P28829). Consensus recognition sequence is indicated above. Key hydrophobic and charged residues are highlighted in colour. Note that the hydrophobic residues are part of the hydrophobic core that defines the conformation of the Ras/Rap binding region.

b, Superposition of SHANK3 SPN (cyan) and RalGDS RA (PDB ID 1LFD) (grey) domain structures. Key positively- and negatively-charged side-chains in both proteins are shown as sticks.

c, Electrostatic surface of the SPN domain highlighting the location of positive charges (blue) aligned with key charged residues mediating Ras/Rap interaction with RA domains.

d, SHANK3 SPN WT-GFP, co-expressed with constitutively active (G12V), wild-type (WT), or dominant negative (S17N) HA-tagged H-Ras in HEK293 cells, was immunoprecipitated (IP) from cell lysates, and input lysates and IP samples were analysed using anti-GFP and anti-HA antibodies, as indicated.

e, SHANK3 SPN WT-GFP domain co-expressed with HA-tagged WT and mutant Ras family of G-proteins, as indicated. GFP-containing proteins were IP from cell lysates, and input lysates and IP samples were analysed as in d.

f, Model of the SHANK3 SPN domain in complex with Ras based on the structure of RalGDS/active H-Ras complex (PDB ID 1LFD).

g, WT and mutant SHANK3 SPN constructs co-expressed with constitutively active (G12V) forms of small GTPases H-Ras, Rap1a and Rap1b. GFP-containing proteins were IP from cell lysates and analysed as in d.

h, Quantification of the data in g; binding efficiency for each HA-tagged G-protein was determined as the ratio of IP to input signal. Ratios obtained with different SHANK3 (WT and mutant) SPN constructs were normalized to SPN WT in each condition (n = 5 (H-Ras) or 4 (Rap1a, Rap1b) experiments; Statistical analysis: ANOVA, followed by Dunnett's multiple comparisons test prior to normalization).

i,j, ITC isotherms for the interactions between active GTP-form of Rap1B and SHANK3 SPN-ARR (i), SHANK3 R12C SPN-ARR (j). Solid lines indicate fitting to the single-site-binding model. Active GTP form of Rap1 was produced using non-hydrolysable GTP analogue GMPPCP. Unprocessed original scans of blots are shown in Supplementary Fig 8.

Figure 5 | SHANK3 regulates integrin activation and cell spreading by a Rap1/Ras-dependent mechanism

a, FACS analysis shows that SHANK3 WT-mRFP, but not SHANK3 mutant, overexpression prevents Rap1Q63E-mediated β1-integrin activation in HEK293 cells. Data represent mean ± SEM relative to mRFP and GFP expressing cells (n = 4 independent experiments; 5000 mRFP/GFP-positive cells analysed per experiment).

b,**c**, Representative confocal images (b) and quantification (c) of spreading MDA-MB-231 cells transfected with GFP-Rap1Q63E alone or together with SHANK3 WT-mRFP. Staining: F-actin and DAPI (cell nuclei). Middle plane confocal image is shown. Scale bar: 10 μm. Tukey box plots represent median cell area relative to untransfected cells (n = 26, 21, 27 cells from left to right from three independent experiments).

d,e, Representative confocal images (d) and quantification (e) of filopodia in rat hippocampal neurons plated on laminin. Staining: F-actin and Map2 (neurite marker). Tukey box plots are shown (n = 176 (WT), 120 (L68P) from two independent experiments). Scale bar = 20 μm (original image) and 10 μm (ROI).

f,g, Representative confocal images (f) and quantification (g) of filopodia in SK-N-BE-2 neuroblastoma cells plated on laminin and differentiated with retinoid acid (10 μM, three days). Shank3 SPN WT-GFP overexpression reduces filopodia density in neurites. Tukey box plots are shown (n = 76 (GFP), 62 (WT), three independent experiments). Scale bar = 20 μm.

h, FACS analysis of β1-integrin activity in *SHANK3*-silenced HEK293 cells treated with a Rap1 inhibitor (10 μM, 1 h). (f) Data are mean ± SEM (n = 5 independent experiments; 10000 cells per experiment).

i,j, Representative images (i) and Image J quantification (j) of cell area in *SHANK3*-silenced HEK293 cells ± Rap1 inhibitor (10 μM, 1 h). Cells were adhering on a fibronectin-collagen matrix (15 min). Middle plane confocal image is shown. Scale bar = 10 μm. Data are represented by Tukey box plots (n = 30, 33, 38 cells from left to right from two independent experiments.

Tukey box plots represent median and 25^{th} and 75^{th} percentiles (interquartile range); points displayed as outliers if 1.5 times above or below the interquartile range; outliers are represented by dots. Statistical analysis: Student's t-test. Statistics source data can be found in Supplementary Table 3.

Figure 6 | Loss of Shank3 promotes active Rap1 localisation to the cell edge.

a, Representative images and quantification of colocalization between Shank3 and constitutively active Rap1 (n = 18 cells from 3 independent experiments). R: Pearson's correlation coefficient. Scale bar = 20 μm (original image) and 10 μm (ROI). **b**, Subcellular membrane fractionation showing increased Rap1 in the membrane fraction of *SHANK3*-silenced HEK293 cells. Representative blots are shown (numbers indicate mean ± SEM from three independent experiments).

c-e, HEK293 cells transiently expressing Raichu-Rap1 FRET probe (imaged for YFP and CFP on a confocal microscope) showing higher Rap1 activity (higher FRET ratio) at the cell periphery of *SHANK3*-silenced cells as compared to control-silenced cells. Representative images (left panels: YFP fluorescence; right panels: FRET ratio; scale bar = 10 μm) are shown (c). FRET ratio at the cell edge and cell body quantified using ImageJ software are presented as Tukey box plots (n = 23 cells from three independent experiments) (d) and the distribution of the FRET signal (mean ± SD; four diametric a-b measurements / cell, n = 252 measurement from three independent experiment) is shown (e).

Tukey box plots represent median and 25^{th} and 75^{th} percentiles (interquartile range); points displayed as outliers if 1.5 times above or below the interquartile range; outliers are represented by dots. Statistical analysis: Student's t-test. Unprocessed original scans of blots are shown in Supplementary Fig 8.

Figure 7 | SHANK1 and SHANK3 sequester active Rap1 to inhibit RIAM/talin-dependent integrin activation and alter adhesion dynamics

a,b, Representative PLA signal (red dots) (a) and quantification of the distribution of the PLA signal relative to the total cell area (F-actin) (b) revealing more co-localization between talin and α5-integrin following SHANK3 silencing in HEK293 cells. Data are displayed as Tukey box plots and expressed relative to control-silenced cells (n = 72 cells from three independent experiments).

c, β1-integrin (P5D2) immunoprecipitation showing enhanced interaction between β1-integrin and talin following SHANK3 silencing in HEK293 cells (representative blot from four independent experiments is shown).

d,e, MDA-MB-231 cells transiently expressing GFP-Talin1 were plated on fibronectin and imaged live using a TIRF microscope (1 picture every 1 min for more than 3 h; scale bar = 20 μm (original image) and 10 μm (ROI)) (d). The percentage of cells displaying a "talin wave"

was then counted (three biological repeats; 84 siCTRL and 86 siSHANK1 movies analysed) (e).

f,g, MDA-MB-231 cells transiently expressing mEmerald-Paxillin were plated on fibronectin and imaged live using a TIRF microscope (1 picture every 1 min for more than 3 h; scale bar = 20 μm) (f). Focal adhesion lifetime was analysed using the focal adhesion analysis server (see methods) (two biological repeats; over 33 movies per condition analysed; n = 97817 siCTRL and 164092 siSHANK1 adhesions analysed) (g).

Tukey box plots represent median and 25th and 75th percentiles (interquartile range); points displayed as outliers if 1.5 times above or below the interquartile range; outliers are represented by dots. Statistical analysis: Student's t-test. Unprocessed original scans of blots are shown in Supplementary Fig 8.

Figure 8 | SHANK1 and SHANK3 regulate cell migration and invasion

a-e, Random cell migration of MDA-MB-231 cells plated on fibronectin-collagen matrix recorded over 24 h by time-lapse imaging showing that *SHANK1*-silenced cells migrate faster and more randomly than control-silenced cells (a-c). Re-expression of Shank1-GFP in *SHANK1*-silenced cells rescued defects observed in cells migration (d, e). Representative cell tracks over 10 h (a) and quantification of the migration speed (b, d) and directionality (c, e) over 24 h are shown. Data were analysed using the Manual Tracking plugin (ImageJ) and are displayed as Tukey box plots (n = 36 (siCtrl) and 37 (siSHANK1) from three independent experiments (b and c); n = 36, 29, 28 from left to right from three independent experiments (d and e).

f,**g**, Inverted invasion assay showing increased MDA-MB-231 cell invasion upon *SHANK1* silencing. Invasion in collagen plugs supplemented with fibronectin was visualized using a confocal microscope by imaging serial optical sections at 15 μm intervals. Individual confocal images are shown in sequence with increasing penetrance from left to right (f). Invasion was quantified using ImageJ by measuring the fluorescence intensity of cells invading 45 μm or more and expressing this as a ratio of the fluorescence intensity of all cells within the plug. Data are presented as Tukey box plots (g) (n = 6 means from three independent experiments).

h, Schematic representation of SHANK-Rap1–dependent integrin inactivation regulating cell adhesion, spreading, migration and invasion.

Tukey box plots represent median and 25^{th} and 75^{th} percentiles (interquartile range); points displayed as outliers if 1.5 times above or below the interquartile range; outliers are represented by dots. Statistical analysis: Student's t-test.

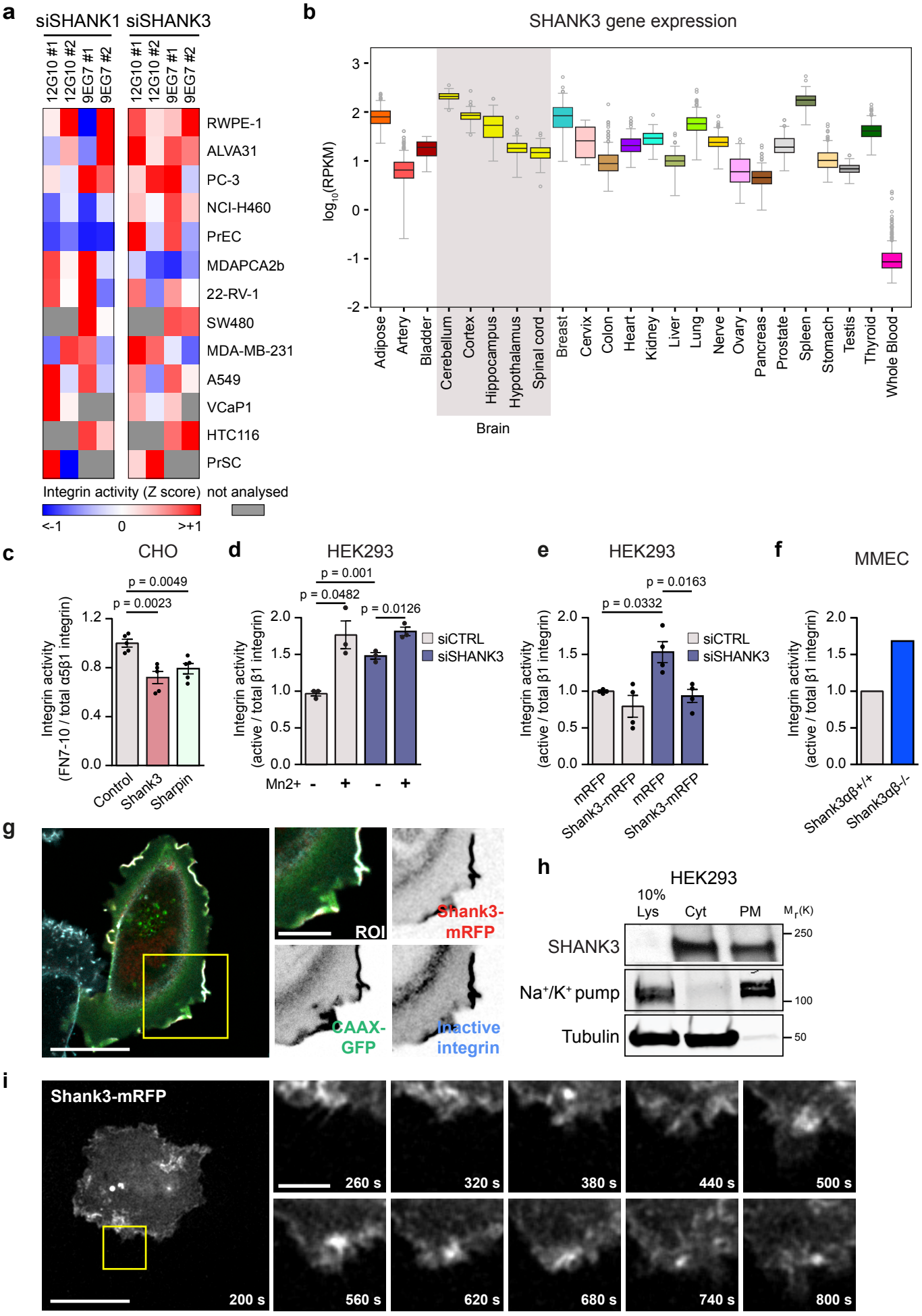
a
siSHANK1
siSHANK3
12G10 #1
12G10 #2
9EG7 #1
9EG7 #2
RWPE-1
ALVA31
PC-3
NCI-H460
PrEC
MDAPCA2b
22-RV-1
SW480
MDA-MB-231
A549
VCaP1
HTC116
PrSC
Integrin activity (Z score)
not analysed
<-1
0
>+1
b
SHANK3 gene expression
log10(RPKM)
Adipose
Artery
Bladder
Cerebellum
Cortex
Hippocampus
Hypothalamus
Spinal cord
Breast
Cervix
Colon
Heart
Kidney
Liver
Lung
Nerve
Ovary
Pancreas
Prostate
Spleen
Stomach
Testis
Thyroid
Whole Blood
Brain
c
CHO
p = 0.0049
p = 0.0023
Integrin activity (FN7-10 / total α5β1 integrin)
Control
Shank3
Sharpin
d
HEK293
p = 0.001
p = 0.0482
p = 0.0126
Integrin activity (active / total β1 integrin)
siCTRL
siSHANK3
Mn2+
e
HEK293
p = 0.0163
p = 0.0332
Integrin activity (active / total β1 integrin)
siCTRL
siSHANK3
mRFP
Shank3-mRFP
f
MMEC
Integrin activity (active / total β1 integrin)
Shank3αβ+/+
Shank3αβ-/-
g
ROI
Shank3-mRFP
CAAX-GFP
inactive integrin
h
HEK293
10% Lys
Cyt
PM
Mr(K)
SHANK3
Na+/K+ pump
Tubulin
250
100
50
i
Shank3-mRFP
200 s
260 s
320 s
380 s
440 s
500 s
560 s
620 s
680 s
740 s
800 s

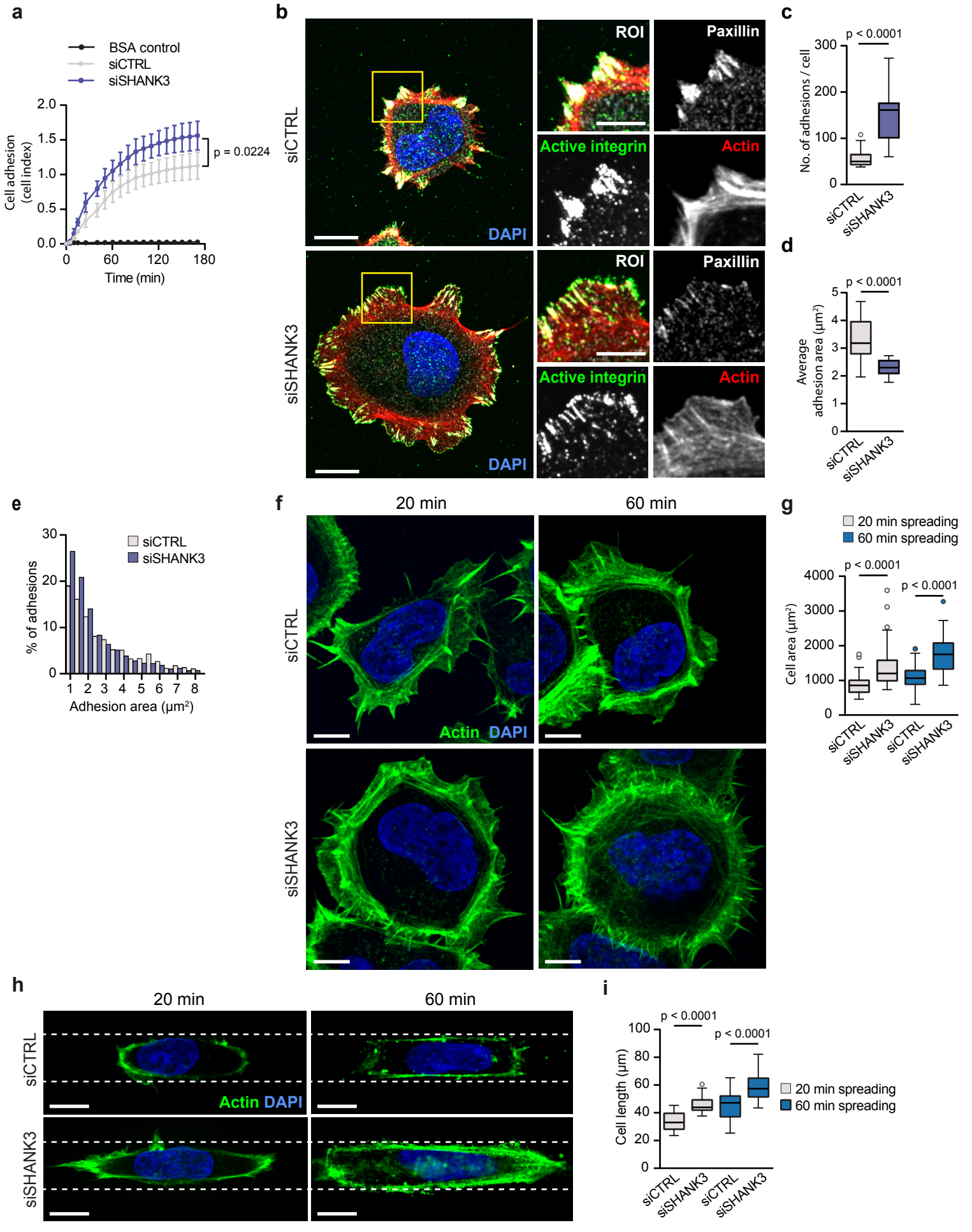
a
BSA control
siCTRL
siSHANK3
Cell adhesion (cell index)
Time (min)
p = 0.0224
b
siCTRL
siSHANK3
ROI
Paxillin
Active integrin
Actin
DAPI
c
No. of adhesions / cell
p < 0.0001
d
Average adhesion area (µm²)
p < 0.0001
e
% of adhesions
Adhesion area (µm²)
f
20 min
60 min
Actin DAPI
g
20 min spreading
60 min spreading
Cell area (µm²)
p < 0.0001
h
Actin DAPI
i
Cell length (µm)
p < 0.0001

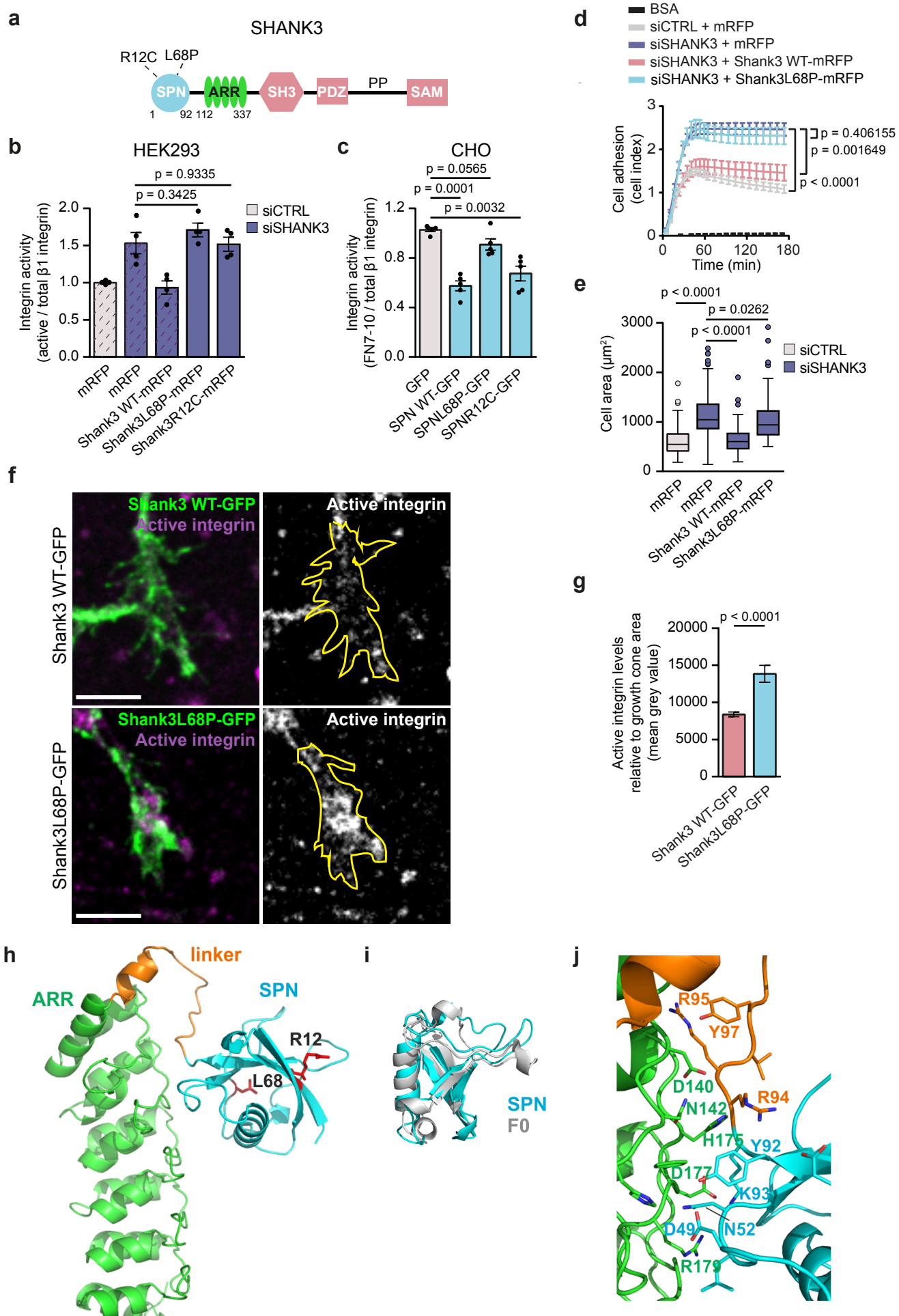
a
SHANK3
R12C
L68P
SPN
ARR
SH3
PDZ
PP
SAM
1
92
112
337
b
HEK293
p = 0.9335
p = 0.3425
siCTRL
siSHANK3
Integrin activity (active / total β1 integrin)
mRFP
mRFP
Shank3 WT-mRFP
Shank3L68P-mRFP
Shank3R12C-mRFP
c
CHO
p = 0.0565
p = 0.0001
p = 0.0032
Integrin activity (FN7-10 / total β1 integrin)
GFP
SPN WT-GFP
SPNL68P-GFP
SPNR12C-GFP
d
BSA
siCTRL + mRFP
siSHANK3 + mRFP
siSHANK3 + Shank3 WT-mRFP
siSHANK3 + Shank3L68P-mRFP
Cell adhesion (cell index)
p = 0.406155
p = 0.001649
p < 0.0001
Time (min)
e
p < 0.0001
p = 0.0262
p < 0.0001
Cell area (μm²)
siCTRL
siSHANK3
mRFP
mRFP
Shank3 WT-mRFP
Shank3L68P-mRFP
f
Shank3 WT-GFP
Active integrin
Shank3L68P-GFP
Active integrin
g
p < 0.0001
Active integrin levels relative to growth cone area (mean grey value)
Shank3 WT-GFP
Shank3L68P-GFP
h
linker
ARR
SPN
R12
L68
i
SPN
F0
j
R95
Y97
D140
R94
N142
H175
Y92
D177
K93
D49
N52
R179

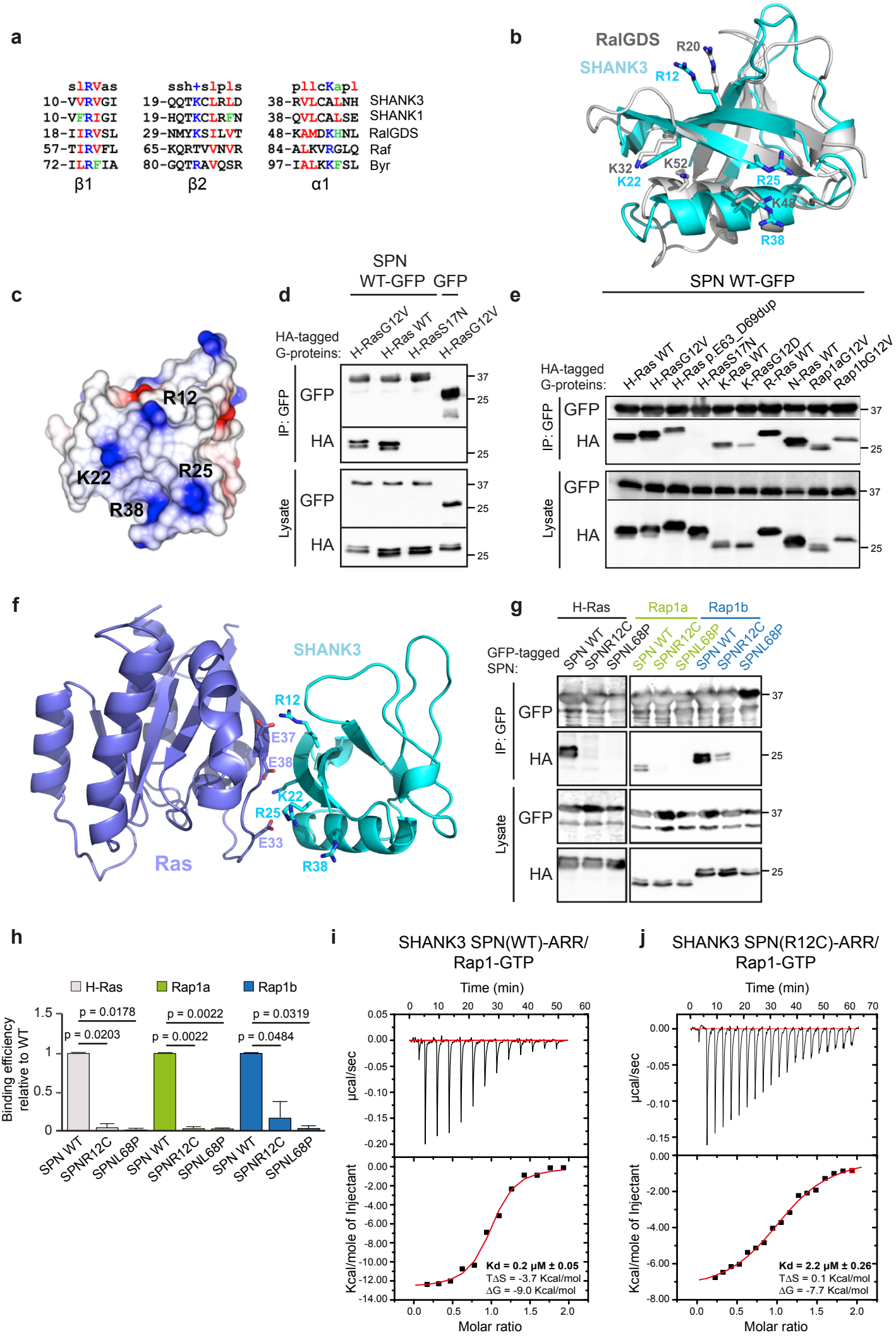
a
slRVas ssh+slpls pllcKapl
10-VVRVGI 19-QQTKCLRLD 38-RVLCALNH SHANK3
10-VFRIGI 19-HQTKCLRFN 38-QVLCALSE SHANK1
18-IIRVSL 29-NMYKSILVT 48-KAMDKHNL RalGDS
57-TIRVFL 65-KQRTVVNVR 84-ALKVRGLQ Raf
72-ILRFIA 80-GQTRAVQSR 97-IALKKFSL Byr
β1 β2 α1
b
RalGDS
SHANK3
R20
R12
K32
K22
K52
R25
K48
R38
c
R12
K22
R25
R38
d
SPN
WT-GFP GFP
HA-tagged G-proteins:
H-RasG12V
H-Ras WT
H-RasS17N
H-RasG12V
IP: GFP
Lysate
GFP
HA
37
25
e
SPN WT-GFP
HA-tagged G-proteins:
H-Ras WT
H-RasG12V
H-Ras p.E63_D69dup
H-RasS17N
K-Ras WT
K-RasG12D
R-Ras WT
N-Ras WT
Rap1aG12V
Rap1bG12V
IP: GFP
Lysate
GFP
HA
37
25
f
SHANK3
R12
E37
E38
K22
R25
E33
R38
Ras
g
H-Ras
Rap1a
Rap1b
GFP-tagged SPN:
SPN WT
SPNR12C
SPNL68P
IP: GFP
Lysate
GFP
HA
37
25
h
H-Ras
Rap1a
Rap1b
Binding efficiency relative to WT
1.5
1
0.5
0
p = 0.0178
p = 0.0203
p = 0.0022
p = 0.0022
p = 0.0319
p = 0.0484
SPN WT
SPNR12C
SPNL68P
i
SHANK3 SPN(WT)-ARR/ Rap1-GTP
Time (min)
µcal/sec
Kcal/mole of Injectant
Molar ratio
Kd = 0.2 µM ± 0.05
TΔS = -3.7 Kcal/mol
ΔG = -9.0 Kcal/mol
j
SHANK3 SPN(R12C)-ARR/ Rap1-GTP
Time (min)
µcal/sec
Kcal/mole of Injectant
Molar ratio
Kd = 2.2 µM ± 0.26
TΔS = 0.1 Kcal/mol
ΔG = -7.7 Kcal/mol

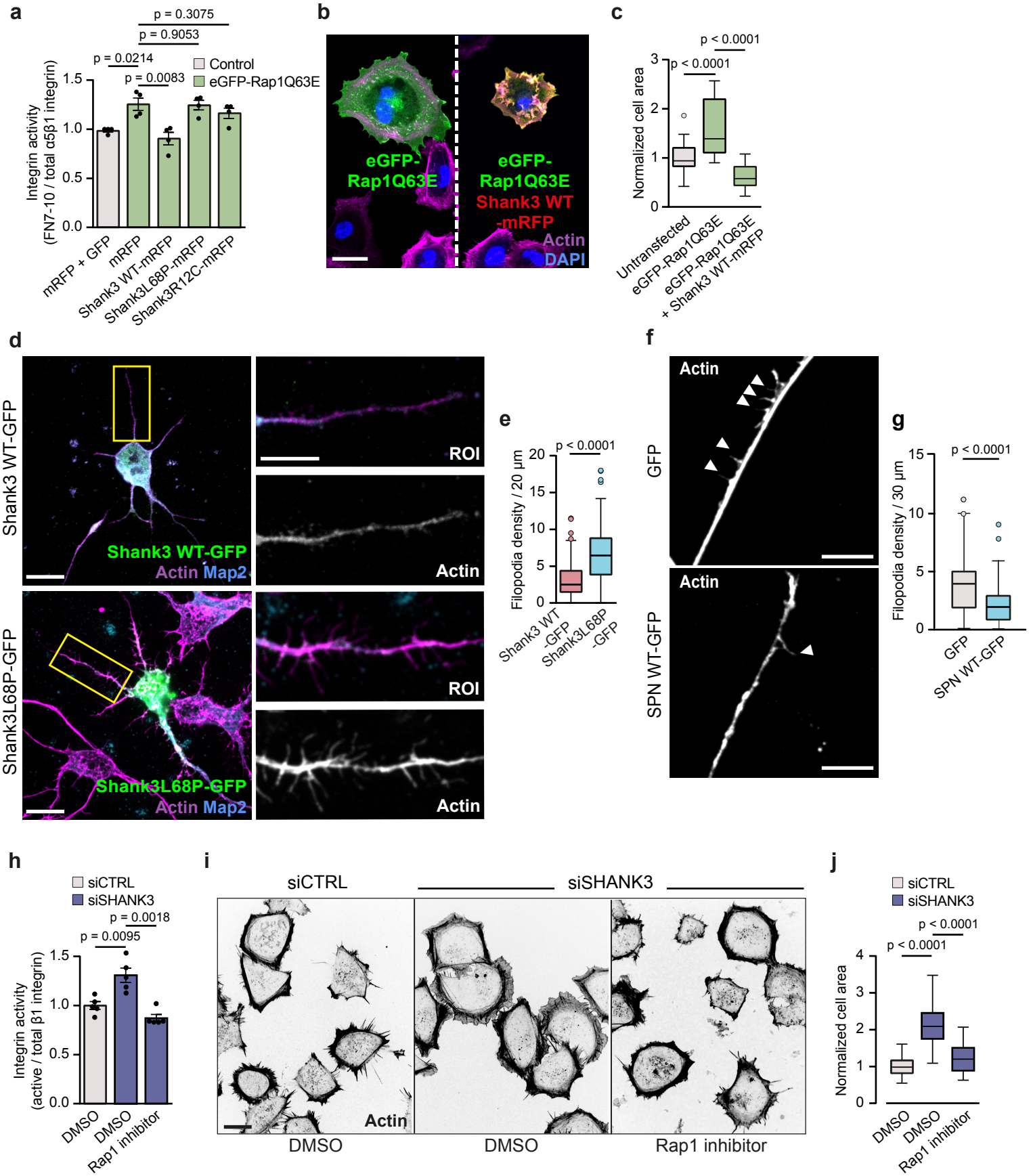
a
p = 0.3075
p = 0.9053
p = 0.0214
p = 0.0083
Control
eGFP-Rap1Q63E
Integrin activity
(FN7-10 / total α5β1 integrin)
1.5
1.0
0.5
0.0
mRFP + GFP
mRFP
Shank3 WT-mRFP
Shank3L68P-mRFP
Shank3R12C-mRFP
b
eGFP-
Rap1Q63E
eGFP-
Rap1Q63E
Shank3 WT
-mRFP
Actin
DAPI
c
p < 0.0001
p < 0.0001
Normalized cell area
3
2
1
0
Untransfected
eGFP-Rap1Q63E
eGFP-Rap1Q63E
+ Shank3 WT-mRFP
d
Shank3 WT-GFP
Shank3 WT-GFP
Actin Map2
ROI
Actin
Shank3L68P-GFP
Shank3L68P-GFP
Actin Map2
ROI
Actin
e
p < 0.0001
Filopodia density / 20 µm
20
15
10
5
0
Shank3 WT
-GFP
Shank3L68P
-GFP
f
Actin
GFP
Actin
SPN WT-GFP
g
p < 0.0001
Filopodia density / 30 µm
15
10
5
0
GFP
SPN WT-GFP
h
siCTRL
siSHANK3
p = 0.0018
p = 0.0095
Integrin activity
(active / total β1 integrin)
1.5
1.0
0.5
0.0
DMSO
DMSO
Rap1 inhibitor
i
siCTRL
siSHANK3
Actin
DMSO
DMSO
Rap1 inhibitor
j
siCTRL
siSHANK3
p < 0.0001
p < 0.0001
Normalized cell area
4
3
2
1
0
DMSO
DMSO
Rap1 inhibitor

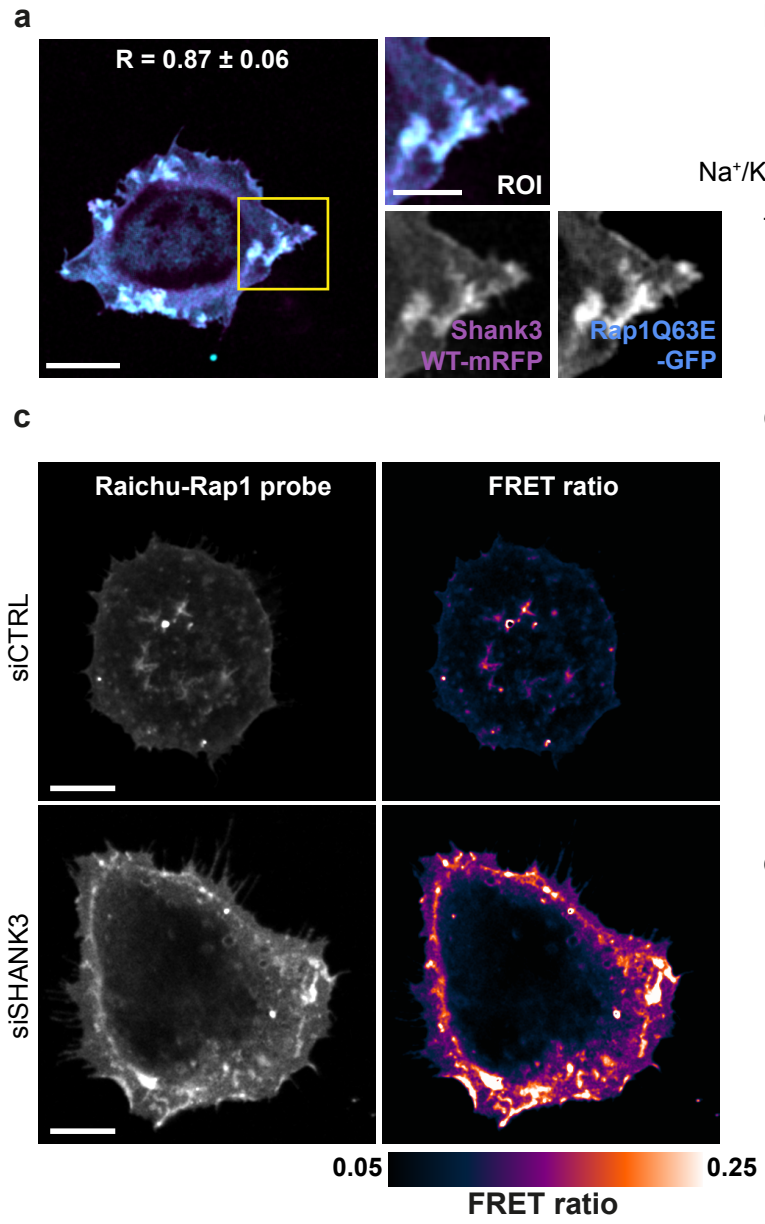
a
R = 0.87 ± 0.06
ROI
Shank3
WT-mRFP
Rap1Q63E
-GFP
b
siCTRL
siSHANK3
Lysate
Lys PM Cyto Lys PM Cyto Mr(K)
Na+/K+ pump
Tubulin
Rap1
100
50
37
1
4.2 ± 2.2
siCTRL
siSHANK3
SHANK3
GAPDH
250
37
c
Raichu-Rap1 probe
FRET ratio
siCTRL
siSHANK3
0.05
0.25
FRET ratio
d
p < 0.0001
p < 0.0001
p < 0.0001
FRET ratio
0.20
0.15
0.10
0.05
0.00
siCTRL
siSHANK3
Cell body
Cell edge
Cell body
Cell edge
e
FRET ratio
siCTRL
siSHANK3
a
b

Lilja et al. Figure 7

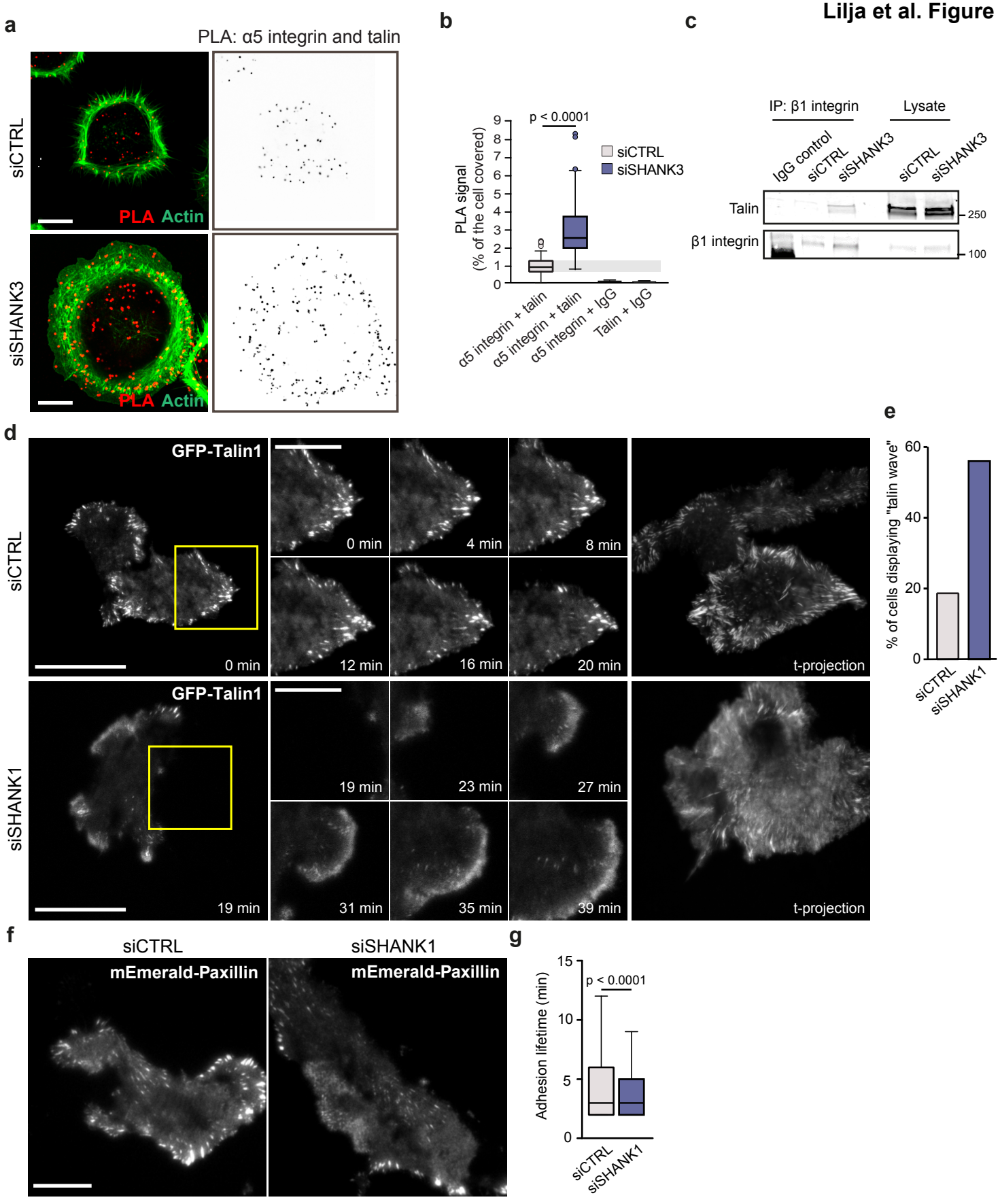

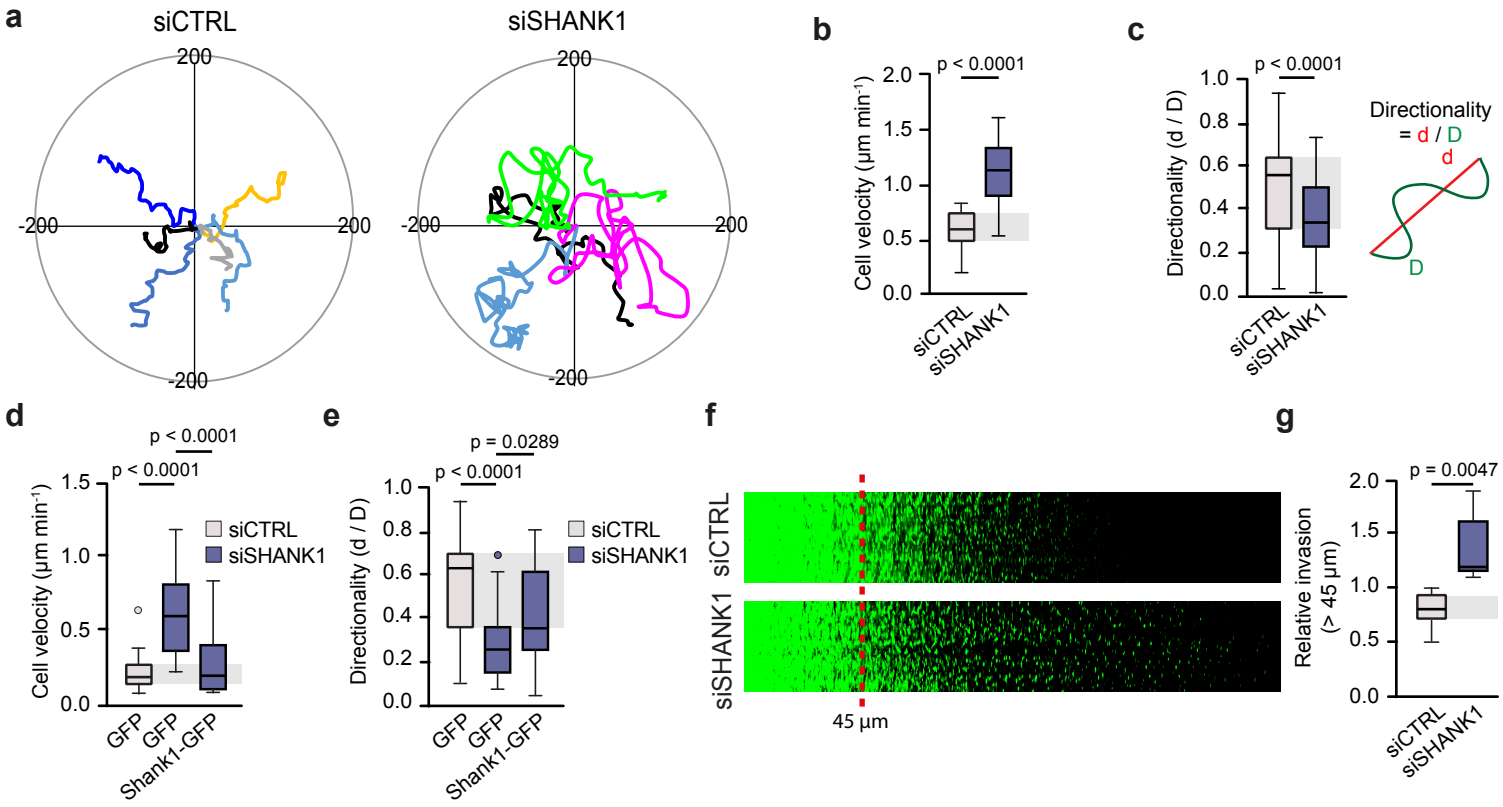
a
siCTRL
siSHANK1
200
-200
b
p < 0.0001
Cell velocity (µm min⁻¹)
siCTRL
siSHANK1
c
p < 0.0001
Directionality (d / D)
Directionality
= d / D
d
D
d
p < 0.0001
p < 0.0001
Cell velocity (µm min⁻¹)
siCTRL
siSHANK1
GFP
GFP
Shank1-GFP
e
p = 0.0289
p < 0.0001
Directionality (d / D)
f
siCTRL
siSHANK1
45 µm
g
p = 0.0047
Relative invasion
(> 45 µm)

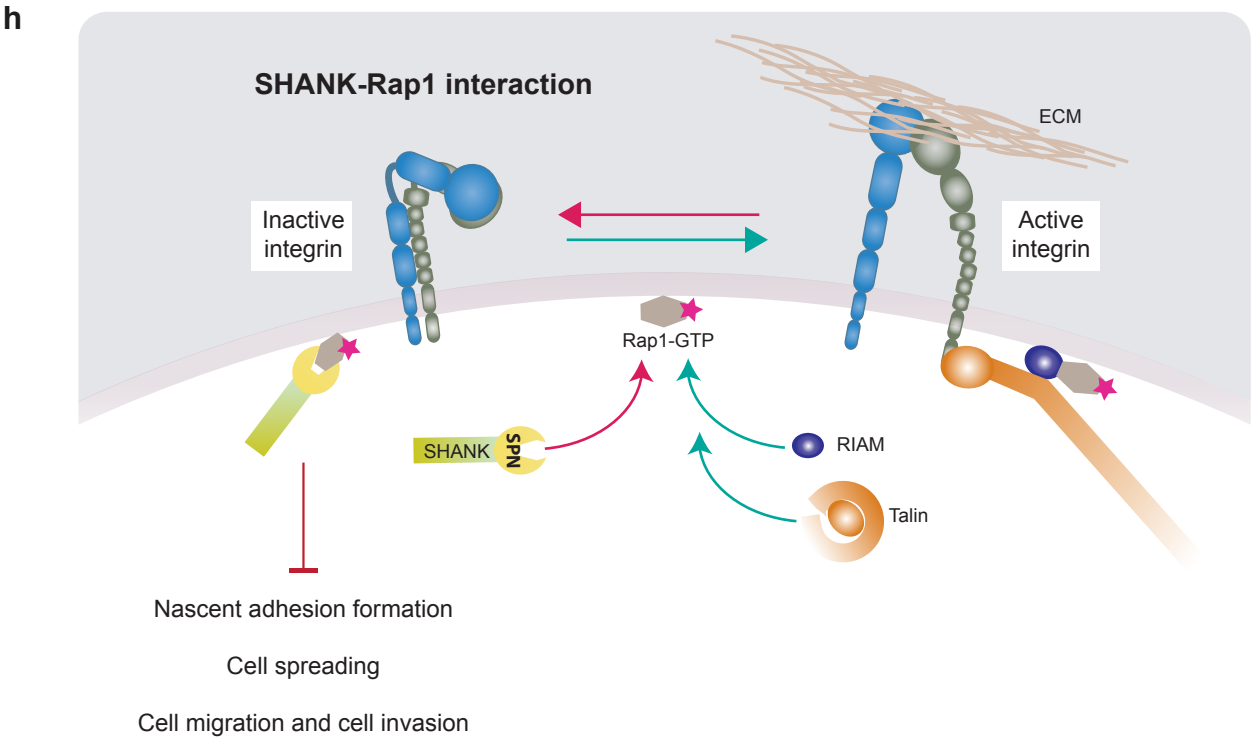
h
SHANK-Rap1 interaction
ECM
Inactive
integrin
Active
integrin
Rap1-GTP
SHANK
NPS
RIAM
Talin
Nascent adhesion formation
Cell spreading
Cell migration and cell invasion

SHANK proteins limit integrin activation by directly interacting with Rap1 and R-Ras

Lilja et al. Online Methods and references

Methods

Cell culture. CHO (Chinese hamster ovary) cells were maintained in Alpha-MEM medium (Sigma-Aldrich) supplemented with 5% fetal bovine serum (FBS, Gibco) and 2 mM L-glutamine (Sigma-Aldrich). HEK293 (human embryonic kidney, ATCC) cells were grown in DMEM (Dulbecco's modified Eagle's medium, Sigma-Aldrich) supplemented with 10% FBS and 2 mM L-glutamine. MDA-MB-231 (triple-negative human breast adenocarcinoma, ATCC) cells were maintained in DMEM supplemented with 10% FBS, 2 mM L-glutamine, and 1% non-essential amino acids (Sigma-Aldrich). Immortalized mouse embryonic fibroblasts (MEFs) isolated from wild-type and *SHARPIN*-null (cpdm) mice have been described previously [7]. MEFs were cultured in DMEM supplemented with 10% FBS, 2 mM L-glutamate, 1 mM sodium pyruvate (Sigma-Aldrich), 1% non-essential amino acids and 1:100000 β-mercaptoethanol (Sigma-Aldrich). SK-N-BE-2 neuroblastoma cells (ATCC) were maintained in DMEM:HAM's F-12 medium supplemented with 10% FBS, 2 mM glutamine and 1% non-essential amino acids. All cells were routinely tested for mycoplasma contamination. No cell lines used in this study were found in the database of commonly misindentified cell lines that is maintained by ICLAC and NCBI Biosample. The cell lines were not authenticated.

Mice and rats. Shank3αβ-deficient mice (*Shank3αβ*$^{-/-}$) were generated by Genoway (Lyon, France) and raised on a C57BL/6 background, as described previously [29]. Mice were kept in conventional open cages in pathogen-free barriers under normal food and lighting conditions. WT and *Shank3αβ*$^{-/-}$ animals were obtained from heterozygous mating. *Shank3αβ*$^{-/-}$ embryos for neuronal culture were obtained from mating of *Shank3αβ*- deficient parents. Animals were genotyped by PCR as described [29]. In experiments using rat neuronal cultures, cells were isolated from Wistar rat (Charles River) embryos. For each experiment, one pregnant rat (4-5 months old) was sacrificed and neurons were prepared from all embryos present, regardless of gender (14-16 embryos). All mouse and rat procedures were performed in compliance with the guidelines for the welfare of experimental animals issued by the Federal Government of Germany and the Finnish Government, and covered by animal license Org766 (Hamburg, Germany) and 20006 (Turku, Finland). All rat experiments were approved by, and conducted in accordance with, the guidelines of the Animal Welfare Committee of the University Medical Center (Hamburg, Germany).

Isolation of mouse mammary gland cells. Primary mouse mammary stromal fibroblasts (MMFs) and mouse mammary epithelial cells (MMEC) were isolated from the mammary

glands of adult (17-25 weeks old) virgin female mice. Briefly, the 2nd, 3rd, 4th and 5th mammary glands from three wild-type and *Shank3αβ*$^{-/-}$ mice per experiment were removed aseptically without lymph nodes, minced with surgical blades, incubated in a shaker for 2 to 3 h at 37 °C in 25 - 30 ml of digestion media (DMEM /F12, 5% FBS, 5 µg/ml insulin, 50 µg/ml gentamicin) containing 2 mg/ml collagenase type XI (Sigma). The cell suspensions were centrifuged 10 min at 400 g to eliminate floating fat cells. Cell pellets were resuspended in isolation media (DMEM/F12, 50 µg/ml gentamicin, pen/strep) with 20 U/ml DNase I (Roche) and incubated for 3 min at room temperature with occasional shaking. Cells were pelleted and disaggregated by pipetting up and down 10 times in 10 ml of isolation media. After each round of pulse centrifugation at 400 g, the supernatant containing single cells was collected and pooled. After four rounds of pulse centrifugation, the pellet containing mammary epithelial ducts was collected. MMECs were trypsinised and pushed through a cell strainer (70 µm, 352350 BD Biosciences) to obtain single cells. The supernatants containing MMFs were also pelleted, and resuspended in fibroblast growth media (DMEM/F12, 5% FBS, L-glutamine, pen/strep). MMEC and MMF cell suspensions were fixed with 4% paraformaldehyde (PFA) for 10 min at room temperature and resuspended in PBS.

Primary neuron culture and transfection. For preparation of primary hippocampal and cortical neurons from E20 rat embryos or E16 *Shank3αβ*$^{-/-}$ mice, embryonic brain tissue was dissected, and neurons were recovered by enzymatic digestion with trypsin and mechanical dissociation. Cells were maintained in Neurobasal medium supplemented with 2% B27 supplement, 0.5 mM L-glutamine, 0.1 mg/mL primocin and 25 µM glutamate (all from Invitrogen). Cells were transfected with pHAGE-EGFP-Shank3 WT or L68P construct using Amaxa Rat neuron nucleofector kit (Lonza).

Transient transfections. Lipofectamine 3000 and P3000™ Enhancer Reagent (Thermo Fisher Scientific Inc) were used for transient plasmid transfections according to manufacturer's protocol and the cells were cultured for 24 h. SiRNA silencing was performed using 100 nM siRNA and Lipofectamine® RNAiMAX Reagent (Thermo Fisher Scientific Inc) according to manufacturer's protocol and cells were cultured for 3 days. The siRNAs targeting human SHANK1 and SHANK3 were SMARTpool ON-TARGETplus purchased from Dharmacon (SHANK1 Cat. No. L-031945-02-0005; SHANK3 Cat. No. L-024645-00-0005). SiRNAs used as controls were Allstars negative control siRNA (Qiagen, Cat. No. 1027281) and ON-TARGETplus Non-targeting Pool (Dharmacon, Cat. No. D-001810-10-05). Rescue experiments consisted of plasmid transfections 72 h after siRNA silencing of the protein of interest.

cDNA constructs. Rat Shank3-mRFP WT, Shank3R12C-mRFP, Shank3L68P-mRFP and rat Shank1-GFP were used in this study. WT and mutant (L68P, R12C) rat Shank3/ProSAP2 cDNAs have been described earlier [32]. There are two alternative translation start codons in this cDNA (acc. NM_021675); we refer here to the second start codon as codon 1, so that the codon for Arg12 in the rat Shank3 cDNA corresponds to the (mutated) codon for Arg12 in the human *SHANK3* gene. cDNAs were subcloned into pmRFP-N3 in frame with the mRFP coding sequence for expression of C-terminal mRFP-tagged Shank3 variants. In addition, pHAGE-EGFP-Shank3 (rat) was kindly supplied by Alex Shcheglovitov (Stanford, CA). The L68P mutation was introduced using the QuikChange II mutagenesis kit (Agilent).

For expression of GFP-tagged SPN domain, the sequence coding for the rat Shank3 SPN domain was cloned into pEGFP-C1 (Clontech). For the expression of His6-SUMO-tagged fusion proteins of N-terminal portions of Shank proteins, appropriate cDNA fragments were amplified by PCR using wt or mutant Shank cDNAs as a template, and cloned into pET-SUMO vectors (Champion™ pET SUMO Protein Expression System, Invitrogen). Protein expressed from pET-SUMO-Shank3$_{1\text{-}348}$ was used for crystallization and binding assays. For introduction of a cleavage site for the tobacco etch virus (TEV) protease, cDNA coding for amino acids SSENLYFQGSS was introduced into this vector between codons for Asn100 and Leu101 by a recombinant PCR approach. Human H-Ras was cloned into pOPINJ vector (OPPF-UK) encoding an N-terminal hexa-histidine GST tag followed by 3C protease cleavage site. Rap1 isoform Rap1b (residues 1-166) was cloned into pTAC vector. For cDNAs coding for human Rac1 or cdc42 were amplified by PCR and cloned into a modified pcDNA3 vector (Invitrogen) which codes for an N-terminal T7 epitope. Constitutively active mutants were generated by PCR (initially described in [64]). Human SHARPIN-GFP has been described in [7]. Human constitutively active R-Ras expression clone (pEGFP-R-RasG38V) [48], human constitutively active Rap1A expression clone (CA-Rap1; pEGFP-C3-Rap1Q63E), a gift from B. Baum and S. Royale described in [65], the Raichu-Rap1 FRET probe, a gift from Matsuda M. [56], mEmerald-Paxillin-22, a gift from Michael Davidson (Addgene plasmid # 54219), GFP-Talin1, mRFP and peGFP-C1 were used in this study.

Antibodies, compounds and reagents. Antibodies used in the study are described in Supplementary Table 2. Phalloidin–Atto 647N (65906, Sigma-Aldrich, 1:400) and Alexa Fluor® 488 Phalloidin (A12379, Life Technologies, 1:100) were used to stain filamentous actin. AlexaFluor-conjugated secondary antibodies (488, 555, 633, 647-conjugated anti-mouse, rabbit, goat, chicken and rat antibodies, Life Technologies) were used in immunofluorescence (1:300 or 1:1000 (anti-chicken)) and FACS (1:200). The 4′6-diamidino-

2-phenylindole (DAPI, Life Technologies 1:10000) or DAPI-containing mounting medium (ProLong Diamond Antifade Mountant with DAPI, Thermo Fisher) were used for nuclear staining. The bovine plasma fibronectin (341631) was obtained from Merck. The collagen from calf skin (C8919), poly-L-Ornithine solution (P4957) and laminin were obtained from Sigma-Aldrich. The laminin-521 was obtained from BioLamina. Rap1 inhibitor, G5169-GGTI 298 trifluoroacetate salt hydrate (Sigma-Aldrich), was dissolved in sterile DMSO.

High-density cell spot microarray (CSMA) screening and Clustergram. The CSMA screening is described in [22]. Here, the results of integrin activation using SHANK1 and SHANK3 siRNAs are shown. Z-scores were hierarchically clustered on the basis of uncentred Pearson correlation using Cluster 3.0 (C Clustering Library, version 1.50) [66] and visualized using Java TreeView (version 1.1.6r2) [67]. RWPE1: immortalized prostate cell line; PrEC, PrSC: primary prostate cells; ALVA31, PC3, MDA-PCA2b, 22-RV1 and VCaP1: prostatic cancer cell lines; A549 and NCI-H460: lung carcinoma cells; MDA-MB-231: breast carcinoma cell line; HTC116 and SW480: colon carcinoma cell lines.

GTEx portal analysis. *SHANK3* gene expression in human tissues was analysed using the publicly available genotype-tissue expression (GTEx) portal (http://www.gtexportal.org/home/gene/SHANK3).

Quantitative real-time polymerase chain reaction (qPCR). Total cellular RNA was extracted using the NucleoSpin® RNA kit (Macherey-Nagel) and 1 µg of the extracted RNA was used as a template for cDNA synthesis by high-capacity cDNA reverse transcription kit (Applied Biosystems) according to the manufacturer's protocol. Expression levels of SHANK 1 and 3 were determined by TaqMan® qPCR reaction using Real-Time PCR HT7900 (Applied Biosystems). Level of glyceraldehyde 3-phosphate dehydrogenase (GAPDH) expression was used as a reference (endogenous control). Taqman® Universal Master Mix II included necessary components for qRT-PCR reaction. The following primers from Sigma were used for human samples: SHANK1 (forward CTCCCTGCGTTCCAAATGTA, reverse GGCTGCTGCTCGTACTCC, Universal ProbeLibrary probe#25); SHANK3 (forward TTCCACGGACCAAGTCTGTA, reverse GTCTTGCATCGAGGTGCTC, probe #11); human GAPDH (forward GCTCTCTGCTCCTCCTGTTC, reverse ACGACCAAATCCGTTGACTC, probe #60). Relative expression was calculated by the 2ΔΔCT method using the expression level of GAPDH as a reference for the quantification.

Western blot assay. Protein extracts were separated on SDS-PAGE under denaturing conditions (4-20% Mini-PROTEAN®TGX Gels, Bio-Rad) and transferred to nitrocellulose membrane. Membranes were blocked with 5%-milk-TBST and incubated with the indicated primary antibodies overnight at 4C followed by fluorophore-conjugated or Amersham ECL HRP-linked secondary antibodies at room temperature for 1 h. Membranes were scanned using an Odyssey infrared imaging system (Odyssey; LI-COR Biosciences) or Amersham ECL Plus™ Western blotting reagent was used and film was developed. Band intensity was determined using ImageJ software.

Flow cytometry assays for β1-integrin activity. The flow cytometry assay analysing labelled fibronectin (fibronectin) repeat 7-10 binding as a measure of active cell-surface β1-integrin levels, was performed as described earlier [23, 24]. Cells were detached with Hyclone® HyqTase (cat: SV300.30.01, Thermo Fisher Scientific Inc) and washed once with full medium containing 10% FBS. The cells were suspended in 100 µl of 37^{o}C serum-free medium with (1) 1:50 Alexa Fluor 647 -labelled fibronectin fragment 7-10 (fibronectin7-10), (2) 1:50 fibronectin7-10 supplemented with 5 mM EDTA (the negative control) or (3) total β1-integrin antibody (PB1 for hamster cells, P5D2 for human cells, MAB1997 for mouse cells) and 1:200 Alexa-647 conjugated secondary antibody. Cells were incubated with rotation for 40 min at room temperature. After washing once with cold tyrodes buffer (10 mM Hepes-NaOH pH 7.5, 137 mM NaCl, 2.68 mM KCl, 0.42 mM NaH_2PO_4, 1.7 mM $MgCl_2$, 11.9 mM $NaHCO_3$, 5 mM glucose, 0.1% BSA), the cells were fixed with 4% PFA in PBS for 10 min at room temperature.

For antibody-based analysis of active β1-integrin cell-surface levels, the flow cytometry assay was performed as described earlier [68]. Briefly, PFA-fixed cells were washed with cold Tyrodes buffer and stained with active β1-integrin specific antibody (1:100 9EG7 for human/mouse cells) or total β1-integrin antibody (P5D2 for human and Mab1997 for mouse cells) for 1 h at 4^{o}C. Cells were washed with Tyrodes buffer and followed by incubation with fluorescently conjugated secondary antibody for 1 h at 4^{o}C. The negative control cells were stained only with secondary antibody. All antibodies were diluted into Tyrodes buffer. The fluorescence was measured by flow cytometry (FACScalibur or LSRFortessa, BD Biosciences, Franklin Lakes, NJ). The median fluorescence intensity was measured from 5000 – 20000 events. Viable, single cells were gated by forward scatter (FSC) and side scatter (SSC) dot blot (Flowing Software 2.5.1). In experiments using mRFP and/or GFP constructs the mRFP and/or GFP expressing cells were gated (5000 positive cells per sample) and analysed for APC (Alexa 647) intensity.

Membrane fractionation. Adherent cells (one 10 cm dish per condition) were washed with PBS and scraped in 500 µL of hypotonic lysis buffer (10 mM HEPES-KOH pH 7.2, 0.25 M sucrose, 1 mM EDTA, 1 mM MgOAc and protease and phosphatase inhibitors (Complete and PhosSTOP tablets from Roche)). Cells were fragmented about 20 times with a French press and 40 µL of total lysate was saved. The remaining lysate was centrifuged at 1000 g for 10 min to remove nucleus and cell debris. The supernatant was then centrifuged at 10000 g to collect total membrane fraction (pellet) and cytosolic fraction (supernatant). Membrane fraction was washed at least once with lysis buffer and cytoplasmic fraction was centrifuged twice. All fractionation steps were performed at 4°C or on ice. All fractions were dissolved in sample buffer for immunoblotting and analysed by SDS–PAGE followed by western blotting with the indicated antibodies.

Adhesion assay using *xCELLigence* Real-Time Cell Analysis (RTCA). The real-time *xCELLigence* cell analyser RTCA (Roche Diagnostics, Germany) was used to measure cell adhesion over time. RTCA measures the impedance that is expressed as a cell index. Cell index value presents the impedance between electrodes (bottom sensors). The 96-well E-plate (Roche) was coated with fibronectin and collagen or 0.1% BSA (Gibco) in PBS, followed by blocking with 0.1% BSA in PBS, both at 37°C for 1 h. BSA-coated wells were used as negative controls. siRNA-treated and/or transfected cells (HEK293 or MDA-MB-231) were detached with Hyclone® HyqTase, washed with full medium including 10% FBS and 20000 cells/well were seeded on E-plates in serum-free medium. Cell index was measured in real-time.

Cell spreading and immunostaining. siRNA-treated and/or transfected cells (HEK293, MDA-MB-231) were maintained in full medium and were allowed to spread for 20 min or 1 h on glass-bottom dishes (MatTek corporation) previously coated with fibronectin and collagen overnight at 4°C. Transfected SK-N-BE-2 cells were plated on laminin-521-coated glass-bottom dishes and differentiated using 10 µM retinoid acid in full medium for 3 days. To study the role of Rap1 in *SHANK3*-silenced cells, cells were pre-treated with 10 µM Rap1 inhibitor (or DMSO) and plated for 1 h on fibronectin-collagen in the presence of the inhibitor (or DMSO). Cells were fixed with 4% PFA, washed, permeabilised with 0.5% Triton-X-100 for 10 min and blocked with 1 M Glycine for 30 min at room temperature. Cells were washed and then stained with the indicated primary antibodies diluted in PBS (1:100) for 30 min at room temperature. Cells were then washed and incubated with Alexa-conjugated secondary antibodies (1:300), Phalloidin–Atto 647N (1:400) or Alexa Fluor 488

Phalloidin (1:100), and 4′6-diamidino-2-phenylindole (DAPI, nuclei staining, 1:10000) in PBS for 30 min at room temperature.

Transfected neurons were plated at a density of 4000/mm² (hippocampal) or 20000/mm² (cortical) in on 18-mm glass coverslips previously coated with 0.01 % poly-L-Ornithine solution (Sigma-Aldrich) for 1 hr at room temperature, followed by 4 µg/ml laminin (Sigma-Aldrich) in PBS overnight. Cultures were maintained at 37 °C, 5% CO_2 in a humidified incubator. Neurons were fixed at DIV1 with 4% paraformaldehyde / 4% sucrose in PBS for 15 min and permeabilised with 0.1% Triton X-100 in PBS for 3 min at room temperature. Rat neurons were blocked with 10% horse serum in PBS for 1 h at room temperature, then incubated with Map2 (Antibodies online; Aachen, Germany; 1:1000 in 2% horse serum) overnight at 4°C, followed by 1 h of incubation at room temperature with Alexa-conjugated secondary antibody (1:1000 in PBS) and with 547-Phalloidine (1:40 in PBS) for 20 min at room temperature. Nuclei were stained with DAPI-containing mounting medium (ProLong Diamond Antifade Mountant with DAPI, Thermo Fisher). Mouse neurons were blocked with 1 M glycine for 30 min at room temperature, washed and stained using indicated primary antibodies diluted in PBS (1:100) for 25 min at RT. Cells were then washed and incubated with Alexa-conjugated secondary antibodies (1:300).

Finally, cells were washed and imaged with a confocal microscope. Cell area was analysed using ImageJ and the number and size of active integrin (9EG7) positive cell adhesions were analysed using the Cell Profiler software. Colocalisation analyses were performed using NIH ImageJ Plugin JACop.

Micropatterns. Micropatterns were produced on glass coverslips as previously described [69, 70]. Cells were seeded on collagen-fibronectin-coated micropattern lines (width 9 µm) for either 20 min or 60 min (cells on line) before fixing with 4% PFA. Samples were stained as described above.

FRET analysis of active Rap1 localization. siRNA-treated HEK293 cells transiently expressing Raichu-Rap1 FRET probe [71, 72] were plated on fibronectin-collagen-coated glass-bottom dishes for 1 h at 37°C. Cells were then fixed in 4% PFA, washed with PBS and blocked in a solution of 1 M glycine for 30 min. Cells were then imaged with a confocal microscope (LSM780, Zeiss) using an 63x (NA 1.2 W) objective. The ZEN imaging software was used to generate and export the Fc images with intensities converted from the FRET index calculated for each pixel using the Youvan method. FRET ratio at the cell edge and cell body was quantified using NIH ImageJ and Cell Profiler software.

Proximity Ligation Assay (PLA). PLA detection of α5-integrin-talin interaction was performed as previously described [68]. Briefly, siRNA-treated HEK293 cells were maintained in full medium and were allowed to spread for 20 min on glass-bottom dishes (MatTek corporation) previously coated with fibronectin-collagen overnight at 4°C. The coverslips were washed with PBS, fixed with 4% PFA for 15 min, washed twice with PBS and permeabilised with 0.5% Triton-X-100 in PBS for 15 min at room temperature. Cells were stained using indicated primary antibodies diluted in PBS (1:100) for 1 h at room temperature. Proximity ligation was performed according to the manufacturer's instructions (Duolink *in situ* PLA, Sigma-Aldrich). PLA signals were detected with a spinning disc confocal microscope (Marianas spinning disk imaging system, Intelligent Imaging Innovations, Inc.) using 100x objective (NA 1.4 Oil, Plan-Apochromat, M27) and analysed with NIH ImageJ.

Live-cell imaging. To analyse the dynamics of focal adhesions, cells were transfected with mEmerald-Paxillin (a gift from Michael Davidson, Addgene plasmid # 54219) and plated for at least 6 h on fibronectin-collagen before being imaged live on a TIRF microscope, at 37°C, in presence of 5% CO_2. Images were acquired every minute for at least 3 h, using a 63x (NA 1.46 Oil, alpha Plan-Apochromat, DIC) objective and an internal Optovar (1.6x magnification). Acquired videos were pre-processed using ImageJ and in particular, the contrast was adjusted and a smooth filter was applied. Focal adhesion lifetime was then analysed by uploading the videos to the focal adhesion analysis server (FAAS; http://faas.bme.unc.edu/) [73] using the following settings: detection threshold, 2; Min Adhesion Size, 2 pixels; Min FA, Phase Length (8 min); Min FAAI Ratio, 3.

To analyse the dynamics of talin-containing adhesions, cells were transfected with GFP-Talin-1 and plated on fibronectin-collagen before being imaged live on a TIRF microscope, at 37°C, in the presence of 5% CO_2. Images were acquired every minute for at least 3 h, using a 63x (NA 1.46 Oil, alpha Plan-Apochromat, DIC) objective and an internal Optovar (1.6x magnification).

To visualise Shank3 dynamics, cell were transfected with Shank3-mRFP and plated on fibronectin-collagen and imaged live on a spinning disk microscope, at 37°C, in the presence of 5% CO_2. Images were acquired every 10 seconds for about 10 min, using a 100x (NA 1.4 Oil, Plan-Apochromat, M27) objective and Evolve 512 EMCCD camera (Photometrics, Arizona, U.S.).

Cell migration. siRNA-treated and/or transfected cells (MDA-MB-231 or HEK293) were seeded on fibronectin-collagen and allowed to spread for 4 h. Cells were maintained at 37°C and 5% CO_2 and cell migration was monitored using a TIRF microscope (10x objective). Point visiting was used to allow multiple positions to be imaged within the same time course and images were acquired for 24 h (one picture every ten minutes). To assess cell migration, speed and directionality, cells were tracked using the Manual Tracking plug-in of NIH ImageJ software. Results were computed and analysed by the NIH ImageJ plug-in Chemotaxis Tool.

Inverted invasion assay. Inverted invasion assay was performed as previously described [74]. In brief, 200 µl of collagen I (5 µg/ml; PureCol® EZ Gel, Cat. #5074-G, Advanced BioMatrix Inc., SanDiego, CA, USA) supplemented with 25 µg/ml fibronectin was allowed to polymerize in each transwell chamber, i.e. insert (ThinCert™, pore size 0.8 µm, Greiner bio-one) for 1 h at 37°C. Transwells were then inverted, and 100000 MDA-MD-231 cells in full medium were seeded directly onto the underside of each transwell filter. The droplets of cell suspension were covered and incubated for 4 h at 37°C in a humidified incubator to allow cells to attach to the membranes. Transwell chambers were then washed with serum-free medium to remove serum. Finally, transwells were placed in serum-free medium, and medium supplemented with 10% FCS was placed on top of the collagen plug to make a chemoattractant gradient. Transwells were incubated at 37°C for 72 h. Then, collagen plugs were fixed with 4% PFA for 2 h and stained for actin (Åtto Phalloidin 647) to visualize cells. The plugs were imaged by confocal microscopy (Zeiss LSM510 META) controlled by the Zen2009 Systems Software (Carl Zeiss). Serial optical sections were imaged at 15 µm intervals with a 20x objective lens (NA 0.50 air, Plan-neofluar). Invasion was quantified using the area calculator plugin in ImageJ to measure fluorescence intensities of cells as a ratio of cells invading 45 µm or more into the collagen plug relative to total amount of cells within the plug.

Microscopy. Confocal images were acquired with a laser scanning confocal microscope LSM780 *(*Carl Zeiss Microscopy, Thornwood, NY) using a 63x (NA 1.2 W) objective; or with a spinning disk confocal microscope (Marianas spinning disk imaging system with a Yokogawa CSU-W1 scanning unit on an inverted Carl Zeiss Axio Observer Z1 microscope, Intelligent Imaging Innovations, Inc., Denver, USA) using a 63x (NA 1.4 Oil, Plan-Apochromat, M27 with DIC III Prism) objective and an Orca Flash 4 sCMOS camera (Hamamatsu Photonics K.K., Hamamatsu City, Japan) or 100x (NA 1.4 Oil, Plan-Apochromat, M27) objective and an Evolve 512 EMCCD camera (Photometrics, Arizona,

U.S.); or with LSM510 META (Carl Zeiss Microscopy, Thornwood, NY) using 20 x objective (NA 0.50 air, Plan-Neofluar); or with a Leica Sp5 confocal microscope using a 63x objective (NA 1.4). Images with a TIRF microscope (Zeiss Laser-TIRF 3 Imaging System, Carl Zeiss) were acquired using a 10x objective (NA 0.25 air) or a 63x (NA 1.46 Oil, alpha Plan-Apochromat, DIC) objective with an internal Optovar (1.6x magnification) and an EMCCD camera (Hamamatsu ImageEM C9100-13; Chip size 512x512; Hamamatsu Photonics K.K., Hamamatsu City, Japan). Quantitative analysis for images was performed using ImageJ or Cell Profiler software.

Immunoprecipitation of GFP-tagged proteins. HEK293 cells were transiently transfected with GFP-tagged Shank3 SPN constructs and αT7 or HA-tagged small G-proteins. Cells were lysed using IP buffer (50 mm Tris/HCl, pH 7.5, 120 mm NaCl, 0.5% Nonidet P-40, 1 mm EDTA, plus protease inhibitors pepstatin, leupeptin, and trasylol), cleared by centrifugation, and subjected to immunoprecipitation of GFP-tagged fusion proteins using GFP-trap matrix (Chromotek, Munich, Germany). Input and precipitate samples were analysed by Western blot. Bands were quantified by chemilumiscence, using a BioRad imager and ImageLab software (BioRad). For quantification of co-precipitation efficiency, intensity of precipitate signals was divided by input signals. In a second step, the ratio obtained was normalized to that obtained with SPN WT domain.

Immunoprecipitation of endogenous proteins. Cells were detached with trypsin, spin down and excess liquid was removed. A total of 200 µL of lysis buffer (40 mM Hepes-NAOH, 75 mM NaCl, 2 mM EDTA, 1% NP40 and protease and phosphatase inhibitor tablets) was added (per 10 cm plate). Tubes containing the lysates were rotated for 30 min at 4^{o}C. Lysates were then spin down at 13000 rpm (~16000 g) for 10 min at 4^{o}C and debris were discarded. A total of 20 µL of supernatant was frozen as lysis control. The remainder of the sample was moved to new 1.5 ml tubes and 1.5 µg of antibodies added per sample. The tubes were then incubated overnight at 4^{o}C. Lysates were immunoprecipitated with protein G Sepharose 4 Fast Flow beads (GE Healthcare) for 1 h at 4^{o}C. Finally, immunoprecipitated complexes were washed three times with wash buffer (20 mM Tris-HCl pH 7.5, 150 mM NaCl, 1% NP-40) followed by elution in reducing Laemmli buffer and denatured for 5 min at 95^{o}C for western blotting.

Rap1 activity assay. The level of active Rap1 in control and *SHANK3*-silenced cells was analysed using the Active Rap1 Pull-Down and Detection Kit (Thermo Fisher). SiRNA transfected HEK293 cells were lysed and active Rap1 binding to purified GST-RalGDS Rap-

binding domain (RBD) was analysed according to manufacturer's instructions using pull-downs followed by western blot detection.

Sample preparation for structural and ITC binding analysis. Rat SHANK3 (residues 1-348) was expressed using BL21 competent cells (Invitrogen) cultured in LB (Luria Broth) for crystallization and ITC, or M9 minimal medium for NMR analysis. Cells were grown at 37^{o}C in LB media supplemented with antibiotics to an OD_{600}, cells were cooled to 18^{o}C and induced using 300 μM IPTG (Isopropyl β-D-1-thiogalactopyranoside) for 16 h. Cells were pelleted by centrifugation and resuspended in 20 mM Na_2HPO_4 pH 7.4, 500 mM NaCl and 25 mM imidazole, cells were then treated with protease cocktail inhibitor VII (Calbiochem) and bovine deoxyribonuclease (1 mg/ml) before being lysed using a French Press. Proteins were purified using nickel-affinity chromatography with a linear gradient of lysis buffer containing 500 mM imidazole. SUMO tag was cleaved with recombinant His-tagged sumo protease and removed by a reverse pass on the Ni-NTA column. Following this step the SHANK3 was shown to have > 95% purity by SDS-PAGE chromatography. SHANK3 was then exchanged into 20 mM Tris pH 7.4, 150 mM NaCl, 2 mM DTT (dithiothreitol) and concentrated to 6 mg/ml for crystallization experiments. H-Ras was expressed using Rosetta *pLacI* (Invitrogen) cells and purified using nickel affinity chromatography as described for SHANK3. The GST tag was cleaved with recombinant his-tagged 3C protease and removed by a reverse pass on the Ni-NTA column. H-Ras required subsequent purification using anion exchange purification using a QFF column (GE healthcare) and was shown to be > 95% pure by SDS-PAGE chromatography. Rap1b was expressed in *E. coli* strain CK600K. Cultures were grown at 37^{o}C to OD_{595} of 0.8 and then induced with 200 μM IPTG at 18^{o}C overnight. Protein was purified by ion exchange, followed by gel filtration, as described in [75]. Active GTP form of Ras and Rap1b was produced by nucleotide exchange as described in [76] using non-hydrolysable GTP analogue GMPPCP. GDP form was generated by overnight incubation of GTPase in the presence of 50 fold molar excess of GTP in the presence of EDTA to remove magnesium, followed by the buffer exchange using PD10 column (GE healthcare). Completeness of the exchange was validated by NMR spectroscopy.

X-ray crystallography. Sparse matrix crystal screening of SHANK3 (1-348) was performed using an innovadyne nanodrop screen maker at protein concentration of 6 mg/ml with a 200 nl drop size (1:1 ratio) using sitting drop vapour diffusion. Crystals typically appeared in over 20 conditions overnight, and thus optimization was not necessary. High resolution data was collected on crystals grown in 0.1 M HEPES pH 7.5, 0.4 M K/Na tartrate and were vitrified using 30% ethylene glycol, 10% isopropanol. An 180^{o} wedge of data was collected at

Diamond Light Source (I04-1) with a non-overlapping 0.5° oscillation width. Owing to systematic absences the data was indexed (Pointless) and integrated (MOSFLM) in $p4_12_12$ and then scaled (SCALA). Molecular replacement was performed using PHASER examining all enantiomorphs, implementing a fragment from an ankyrin repeat module with side chains removed from PDB:1N11. Upon isotropic refinement using PHENIX.refine [77] electron density for the full ankyrin repeat was visible and modelled using COOT [78]. This revealed the presence of the SPN domain in the weighted difference map that was subsequently modelled at 1σ. The fully refined electron density map also revealed a significant amount of ethylene glycol and isopropyl alcohol from the cryo-protectant bound to the structure. These bound molecules were assigned and accounted for in the final refinement. Data reduction and refinement statistics are shown in Supplementary Table 1.

NMR spectroscopy. NMR spectra were collected on a Bruker Avance III 600 and 800 MHz spectrometers equipped with CryoProbes. Experiments were performed at 298 K in 20 mM Tris pH 7.4, 150 mM NaCl, 2 mM DTT, with 5% (v/v) ^2H_2O. Spectra were processed with TopSpin (Bruker).

Isothermal titration calorimetry (ITC). ITC experiments were performed using an ITC-200 (Microcal). ITC titrations performed in 20 mM Tris pH 7.4, 150 mM NaCl, 0.5 mM TCEP (tris-carboxyethyl-phosphine) and 3 mM $MgCl_2$ at 25°C. Data were integrated and fitted to a single-site binding equation using Origin 7 software with integrated ITC module (Microcal).

Statistics and Reproducibility. Statistical testing was determined using the Student's t-test (unpaired two-tailed, unequal variance) or ANOVA (followed by Dunnett's test for multiple comparisons, where appropriate). All experiments were repeated at least three times unless otherwise indicated. N numbers are indicated in the figure legends. P-value of 0.05 was considered as a borderline for statistical significance ($P > 0.05$). P-values are indicated in the figures. The experiments were not randomized. No statistical method was used to determine sample size. Investigators were not blinded to allocation during experiments and outcome assessment except for FACS assays.

Data Availability. Atomic coordinates for the reported crystal structure have been deposited in the Protein Data Bank under the accession code 5G4X. Source data for figures 1e, 2a, 3b, 5a, and supplementary figures S1e, S1f, S2a, S5a and S5b can be found in Supplementary Table 3. All other data supporting the findings of this study are available from the corresponding author on reasonable request.

References

64. Soltau, M., Richter, D. & Kreienkamp, H.J. The insulin receptor substrate IRSp53 links postsynaptic shank1 to the small G-protein cdc42. *Molecular and cellular neurosciences* **21**, 575-583 (2002).
65. Dao, V.T., Dupuy, A.G., Gavet, O., Caron, E. & de Gunzburg, J. Dynamic changes in Rap1 activity are required for cell retraction and spreading during mitosis. *Journal of cell science* **122**, 2996-3004 (2009).
66. de Hoon, M.J., Imoto, S., Nolan, J. & Miyano, S. Open source clustering software. *Bioinformatics* **20**, 1453-1454 (2004).
67. Saldanha, A.J. Java Treeview--extensible visualization of microarray data. *Bioinformatics* **20**, 3246-3248 (2004).
68. Nevo, J. *et al.* Mammary-derived growth inhibitor (MDGI) interacts with integrin alpha-subunits and suppresses integrin activity and invasion. *Oncogene* **29**, 6452-6463 (2010).
69. Azioune, A., Storch, M., Bornens, M., Thery, M. & Piel, M. Simple and rapid process for single cell micro-patterning. *Lab Chip* **9**, 1640-1642 (2009).
70. Alanko, J. *et al.* Integrin endosomal signalling suppresses anoikis. *Nature cell biology* **17**, 1412-1421 (2015).
71. Mochizuki, N. *et al.* Spatio-temporal images of growth-factor-induced activation of Ras and Rap1. *Nature* **411**, 1065-1068 (2001).
72. Niwa, H., Yamamura, K. & Miyazaki, J. Efficient selection for high-expression transfectants with a novel eukaryotic vector. *Gene* **108**, 193-199 (1991).
73. Berginski, M.E., Vitriol, E.A., Hahn, K.M. & Gomez, S.M. High-resolution quantification of focal adhesion spatiotemporal dynamics in living cells. *PloS one* **6**, e22025 (2011).
74. Jacquemet, G. *et al.* RCP-driven alpha5beta1 recycling suppresses Rac and promotes RhoA activity via the RacGAP1-IQGAP1 complex. *The Journal of cell biology* **202**, 917-935 (2013).
75. Herrmann, C., Horn, G., Spaargaren, M. & Wittinghofer, A. Differential interaction of the ras family GTP-binding proteins H-Ras, Rap1A, and R-Ras with the putative effector molecules Raf kinase and Ral-guanine nucleotide exchange factor. *The Journal of biological chemistry* **271**, 6794-6800 (1996).
76. John, J. *et al.* Kinetics of interaction of nucleotides with nucleotide-free H-ras p21. *Biochemistry* **29**, 6058-6065 (1990).
77. Adams, P.D. *et al.* PHENIX: a comprehensive Python-based system for macromolecular structure solution. *Acta crystallographica. Section D, Biological crystallography* **66**, 213-221 (2010).
78. Emsley, P. & Cowtan, K. Coot: model-building tools for molecular graphics. *Acta crystallographica. Section D, Biological crystallography* **60**, 2126-2132 (2004).